



# LUND UNIVERSITY

## III-V Nanowire Array Solar Cells: Optical and Electrical Modelling

Chen, Yang

2018

*Document Version:*

Publisher's PDF, also known as Version of record

[Link to publication](#)

*Citation for published version (APA):*

Chen, Y. (2018). *III-V Nanowire Array Solar Cells: Optical and Electrical Modelling* (1 ed.). [Doctoral Thesis (compilation), Solid State Physics]. Lund University, Faculty of Engineering.

*Total number of authors:*

1

### General rights

Unless other specific re-use rights are stated the following general rights apply:

Copyright and moral rights for the publications made accessible in the public portal are retained by the authors and/or other copyright owners and it is a condition of accessing publications that users recognise and abide by the legal requirements associated with these rights.

- Users may download and print one copy of any publication from the public portal for the purpose of private study or research.
- You may not further distribute the material or use it for any profit-making activity or commercial gain
- You may freely distribute the URL identifying the publication in the public portal

Read more about Creative commons licenses: <https://creativecommons.org/licenses/>

### Take down policy

If you believe that this document breaches copyright please contact us providing details, and we will remove access to the work immediately and investigate your claim.

LUND UNIVERSITY

PO Box 117  
221 00 Lund  
+46 46-222 00 00

# III-V Nanowire Array Solar Cells: Optical and Electrical Modelling

Yang Chen



**LUND**  
UNIVERSITY

DOCTORAL DISSERTATION

which, by due permission of the Faculty of Engineering, Lund University,

Sweden,

will be defended in the Rydberg Hall at the Department of Physics,

on 25<sup>th</sup> May 2018, at 9:15.

*Faculty opponent*

Professor Ray LaPierre

McMaster University, Canada

Organization LUND UNIVERSITY  Author(s) Yang Chen	Document name DOCTORAL DISSERTATION	
	Date of issue	
	Sponsoring organization	
Title and subtitle III-V Nanowire Array Solar Cells: Optical and Electrical Modelling		
Abstract <p>This thesis describes optical and electrical modelling of vertically oriented III-V semiconductor nanowire array solar cells (NWASCs).</p> <p>In the optical studies, three-dimensional electromagnetic modelling was carried out with the scattering matrix method and the finite element method. Shockley–Queisser detailed balance analysis was first applied to a dual-junction NWASC in which both junctions were within the nanowires. A limit for the solar cell efficiency was calculated for various nanowire array geometries and materials. The dimensions giving the highest efficiency limit were determined by applying an optimization method that does not rely on the use of derivatives. The optical response of a nanowire array subcell on top of a planar silicon subcell was then considered. For the optimized geometry with approximately 15 nanowires per square <math>\mu\text{m}</math>, a conformal top contact of transparent conductive oxide led to large absorption losses. It was found that a scheme with a planarized top contact reduced these losses. Furthermore, the benefit of using anti-reflection coatings on top of the planar top contact and on the substrate surface between the nanowires was demonstrated. With such coatings, the number of reflected photons could be reduced by 80%.</p> <p>The full opto-electrical response of a single-junction InP NWASC was also studied by combining optical modelling with drift-diffusion-based electrical modelling. The spatially resolved internal quantum efficiency was used as a tool to understand the position-dependent electron–hole splitting efficiency for various designs of the p-i-n junction within the nanowires. Importantly, it was found that contact leakage is an important loss mechanism. A high-bandgap semiconductor, GaP, is suggested as a material for the n-doped top segment, which increases the total electron–hole splitting efficiency to almost 100%. In addition to this top selective contact, the GaP substrate can be used as a p-doped bottom-selective contact. With the application of both selective contacts, it is possible to improve the open-circuit voltage of InP NWASCs to the Shockley–Queisser (S–Q) open-circuit voltage of 1.02 V.</p> <p>Apart from light absorption and solar cell efficiency calculations, a light-emission model for periodic nanostructures was developed by combining Green’s dyads and the drift-diffusion model. This model takes the Purcell effect into consideration, which makes it possible to calculate both near-field and far-field emission powers.</p>		
Key words Semiconductor solar cell, nanowire array, modelling		
Classification system and/or index terms (if any)		
Supplementary bibliographical information		Language English
ISSN and key title		ISBN 978-91-7753-645-8
Recipient’s notes	Number of pages	Price
	Security classification	

I, the undersigned, being the copyright owner of the abstract of the above-mentioned dissertation, hereby grant to all reference sources permission to publish and disseminate the abstract of the above-mentioned dissertation.

Signature \_\_\_\_\_ Date \_\_\_\_\_

# III-V Nanowire Array Solar Cells: Optical and Electrical Modelling

Yang Chen



**LUND**  
UNIVERSITY

Cover photo by Yang Chen

Paper I © 2016 Springer Nature

Paper II © 2016 IOP Publishing

Paper III © 2017 Optical Society of America

Paper IV © 2017 AIP Publishing

Paper V © 2017 IOP Publishing

Paper VI © 2018 IOP Publishing

Paper VII © 2016 American Chemical Society

The rest of thesis copyright Yang Chen

Division of Solid State Physics

Department of Physics

Lund University

ISBN 978-91-7753-645-1 (print)

ISBN 978-91-7753-646-8 (pdf)

Printed in Sweden by Media-Tryck, Lund University

Lund 2017



MADE IN SWEDEN ■■

Media-Tryck is an environmental-  
ly certified and ISO 14001 certified  
provider of printed material.  
Read more about our environmental  
work at [www.mediatryck.lu.se](http://www.mediatryck.lu.se)

---

One Prophecy Everyday

Day 1

Day 2

Day 3

⋮

Day 7 But I have to Labour.

---

⋮

Day 121 “He rested on the seventh day from all his work which he had made .”

⋮

Day 364

Day 365

Day 366 I tell the truth everyday.

A key to the world we live in

Lucifer Chen

2015.5.10Σ

“ If the universe is the answer,  
what is the question? ”

# Acknowledgements

During the past three and a half years, I have been fortunate enough to work with many talented and outstanding scientists. I am also lucky to have lived and worked in such a friendly city and division.

I would like to express my deep thanks to my main supervisor, Professor Mats-Erik Pistol, for his help in both science and daily life. Your ideas concerning science and life in general are impressive. I still remember the first day you picked me up at Copenhagen Airport and took me to the apartment.

I'm also grateful to my assistant supervisor, Dr Nicklas Anttu, for his patient and careful guidance. I have learned many practical skills from your efficient way of working and from our collaboration. Whenever I came to your office, you always had the time to reply to my questions.

I would also like to express appreciation to my supervisor Professor Lars Samuelson, for providing such a high-quality research setting. I was lucky enough to join the NanoTandem project, which you direct, giving me the opportunity to collaborate with people from different countries. I would also like to thank Professor Magnus Borgström in the same project for his kind explanations of the experimental details.

Working with Dr Pyry Kivisaari was a wonderful experience for me during my PhD studies. His excellent understanding of semiconductor band structure and the drift-diffusion model inspired me.

I also enjoyed my long collaboration with Dr Johannes Svensson. You always give me such useful information. More importantly, you, together with Nicklas Anttu and Neimantas Vainorius, helped me develop another area of my life: board games. Your explanations of the rules were very enjoyable. Thanks also to Irene Geijselaers, Damiano Verardo, Anders Kvennefors, Steven Limpert, Regina



Schmitt and Artis Svilans. Without your participation, I wouldn't have enjoyed these games half as much.

I would like to thank Dr Oliver Höhn and Dr Nico Tucher, who helped me with both science and life during my internship in Germany. I still have some of the good habits and ways of thinking I acquired during that time. I would also like to thank our project manager, Gerda Rentschler, for her kind help regarding life in Germany.

The Friday Nano Optics meetings and Nano Energy meetings at the Division helped me comprehend the scientific research. I learned a great deal from discussions with Prof. Heiner Linke, Prof. Mats-Erik Pistol, Prof. Anders Gustafsson, Prof. Anders Mikkelsen, Prof. Håkan Pettersson, Prof. Tönu Pullerits, Dr Dan Hessman, Dr Niklas Sköld and Dr Nicklas Anttu. Thank you for your support when I was in charge of the Nano Optics meeting. I would also like to express my gratitude to Vishal Jain, Mahtab Aghaeipour and Mohammad Karimi for their organization of previous and ongoing Nano Optics meeting.

I would also like to express my appreciation to our technicians, Johanna Mosgeller and Janne Mårtensson, who were always willing to fix the technical problems with my computer and workstation.

Another exciting part of my life in Lund was organizing “spex” with other people. Thanks to Irene Geijselaers, Vigaile Dagyte, Gaute Otnes and everyone who participated the organization.

Thanks to Ali Nowzari, Neimantas Vainorius, Anette Löfstrand, Linus Ludvigsson and Mahtab Aghaeipour for creating the pleasant atmosphere in our office.

Thanks to Prof. Anders Gustafsson for his kind and patient help when I was a fresh student.

I am also grateful to Dr Zhaoxia Bi, Rong Sun, Zhen Li, Xulu Zeng, Chunlin Yu and Fangfang Yang for their helpful information about Lund.

Thanks to my parents for their support, although they do not really understand much about what I am doing.

Finally, thank you Peilin. Words cannot express how much you mean to me.



# Abstract

This thesis describes optical and electrical modelling of vertically oriented III-V semiconductor nanowire array solar cells (NWASCs).

In the optical studies, three-dimensional electromagnetic modelling was carried out with the scattering matrix method and the finite element method. Shockley–Queisser detailed balance analysis was first applied to a dual-junction NWASC in which both junctions were within the nanowires. A limit for the solar cell efficiency was calculated for various nanowire array geometries and materials. The dimensions giving the highest efficiency limit were determined by applying an optimization method that does not rely on the use of derivatives. The optical response of a nanowire array subcell on top of a planar silicon subcell was then considered. For the optimized geometry with approximately 15 nanowires per square  $\mu\text{m}$ , a conformal top contact of transparent conductive oxide led to large absorption losses. It was found that a scheme with a planarized top contact reduced these losses. Furthermore, the benefit of using anti-reflection coatings on top of the planar top contact and on the substrate surface between the nanowires was demonstrated. With such coatings, the number of reflected photons could be reduced by 80%.

The full opto-electrical response of a single-junction InP NWASC was also studied by combining optical modelling with drift-diffusion-based electrical modelling. The spatially resolved internal quantum efficiency was used as a tool to understand the position-dependent electron–hole splitting efficiency for various designs of the p-i-n junction within the nanowires. Importantly, it was found that contact leakage is an important loss mechanism. A high-bandgap semiconductor, GaP, is suggested as a material for the n-doped top segment, which increases the total electron–hole splitting efficiency to almost 100%. In addition to this top selective contact, the GaP substrate can be used as a p-doped bottom-selective

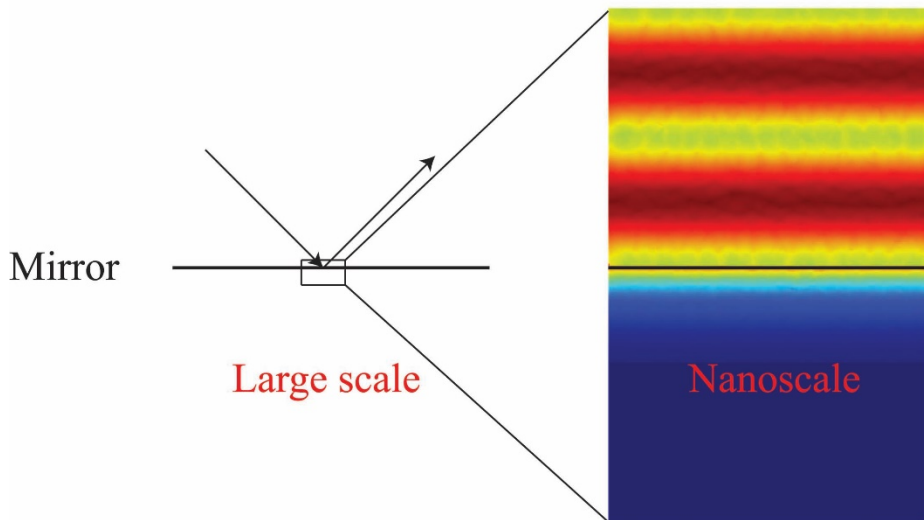
contact. With the application of both selective contacts, it is possible to improve the open-circuit voltage of InP NWASCs to the Shockley-Queisser (S-Q) open-circuit voltage of 1.02 V.

Apart from light absorption and solar cell efficiency calculations, a light-emission model for periodic nanostructures was developed by combining Green's dyads and the drift-diffusion model. This model takes the Purcell effect into consideration, which makes it possible to calculate both near-field and far-field emission powers.

## Popular Scientific Summary

Optics on the nanoscale is quite different from optics in everyday life. For instance, if a beam of light is projected onto a mirror at an incident angle of  $45^\circ$ , it will be reflected at a fixed angle of  $45^\circ$ , according to the law of reflection. However, if we zoom down to the nanoscale level at the mirror, we will see something slightly different.

Firstly, the beam is not a perfect beam with a clear boundary on the nanoscale. It will look like a beam of light coming from a flashlight, no matter how well it is aligned. Secondly, the incident and reflected light disappear at the air-mirror interface, within a distance of several wavelengths, and we will see a series of strange stripes, instead of the clear optical beam.

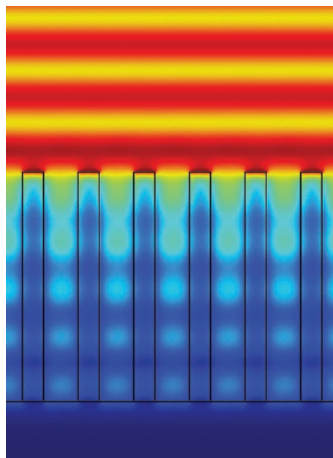


Light reflection on the large scale and the nanoscale. The magnitude of the electric field is shown in the nanoscale plot. Red indicating high intensity and blue low intensity.

Optical waves play tricks on the nanoscale. The incident and reflected light overlap and they are coherent. It is difficult to split them into two beams of light, and the only solution can be found in the form of optical waves. This happens in the close vicinity of the interface, where reflection and transmission take place.

In reality, a bulk surface is not absolutely flat, but has a rough nanostructure. This rough surface scatters light in different directions in a more complicated way. Some of the light can be trapped in the small cavities of the surface, that is to say, the light bounces back and forth many times. This increases the amount of light entering the material.

Scientists can design surfaces with different shapes to make the material absorb more light. In the lab, nanostructures with different shapes can be made with the help of nanotechnology. Nanowire arrays, for example, look like a large number of small pillars standing on flat ground in a uniform way.



**Strong light absorption in a nanowire array. The light intensity of is shown by the colour scale: red indicating high intensity and blue low intensity.**

This “forest” of nanowires helps semiconductors to absorb more light using less material. For instance, such an array can absorb 20 times more photons than the same volume of a planar semiconductor.

The increase in absorption is highly desirable in solar cell applications, especially when using expensive materials such as InP and GaAs. The use of nanowire arrays can significantly reduce the volume of material required in a solar cell, and such an array can absorb a similar amount of sunlight as a thin film.





# List of Papers

This thesis is based on a number of papers, referred to in the text by their Roman numerals.

- I. **Design for strong absorption in a nanowire array tandem solar cell**  
Yang Chen, Mats-Erik Pistol and Nicklas Anttu  
Scientific Reports 6, 32349 (2016)  
I performed the modelling, analysed the results, and wrote the first draft of the manuscript.
- II. **Optimization of the short-circuit current in an InP nanowire array solar cell through opto-electronic modeling**  
Yang Chen, Pyry Kivisaari, Mats-Erik Pistol and Nicklas Anttu  
Nanotechnology, 27, 435404 (2016)  
I performed the modelling with input from P. Kivisaari and N. Anttu, analysed the results, and wrote the manuscript.
- III. **Optical analysis of a III-V-nanowire-array-on-Si dual junction solar cell**  
Yang Chen, Oliver Höhn, Nico Tucher, Mats-Erik Pistol and Nicklas Anttu  
Optics Express, 25, A665 (2017)  
I developed the ideas with O. Höhn, performed the modelling, analysed the results, and wrote the manuscript.
- IV. **Increased Absorption in InAsSb Nanowire Clusters through Coupled Optical Modes**  
Johannes Svensson\*, Yang Chen\*, Nicklas Anttu, Mats-Erik Pistol and Lars-Erik Wernersson  
Applied Physics Letters 110, 081104 (2017)  
\* These authors contributed equally to this work.

I performed most of the modelling and took an active part in the comparison between modelling and experiments. I wrote parts of the manuscript.

V. **Optimized efficiency in InP nanowire solar cells with accurate 1D analysis**

Yang Chen, Pyry Kivisaari, Mats-Erik Pistol and Nicklas Anttu  
Nanotechnology, 29, 045401 (2017)

I developed the codes with P. Kivisaari and N. Anttu, performed the modelling, analysed the results and wrote the manuscript.

**Other related publications**

VI. **Emission enhancement, light extraction and carrier dynamics in InGaAs/GaAs nanowire arrays**

Pyry Kivisaari, Yang Chen and Nicklas Anttu  
Nano Futures, 2, 015001 (2018)

VII. **Dense, Regular GaAs Nanowire Arrays by Catalyst-Free Vapor Phase Epitaxy for Light Harvesting**

Jiehong Jin, Toma Stoica, Stefan Trelenkamp, Yang Chen, Nicklas Anttu, Vadim Migunov, Rudy M. S. Kawabata, Pio J.S. Buenconsejo, Yeng M. Lam, Fabian Haas, Hilde Hardtdegen, Detlev Grützmacher and Beata E. Kardynal  
ACS Applied Materials and Interfaces, 8, 22484 (2016)

VIII. **High-yield Self-catalyzed GaAsSb/GaAs Heterostructured Nanowire Arrays on Silicon for Optoelectronic Applications**

Dingding Ren\*, Junghwan Huh\*, Yang Chen, Julie Nilsen, Dasa Dheeraj, Susanne Sandell, Dong-Chul Kim, Anders Gustafsson, Antonius Van Helvoort, Helge Weman and Bjørn-Ove Fimland  
under review

# Contents

1. General Introduction to Solar Cell Concepts.....	15
1.1. Solar spectra and solar power.....	16
1.2. Absorption of light in semiconductors .....	17
1.3. Extraction of photogenerated charge carriers.....	19
1.4. Energy harvesting with a solar cell, and I-V response .....	20
1.5. Different types of solar cells .....	21
1.5.1. Categorization by concept .....	22
1.5.2. Categorization by material.....	27
1.5.3. Categorization by structure.....	30
2. III-V Nanowire Array Solar Cells .....	31
2.1. Merits of nanowire arrays in solar cell applications.....	32
2.1.1. More freedom in lattice matching .....	32
2.1.2. Enhanced absorption and cost-effectiveness .....	33
2.2. Nanowire array solar cell designs .....	33
3. Optical modelling of nanowire array solar cells.....	37
3.1. Methods of solving Maxwell's equations .....	38
3.1.1. Optical properties of semiconductors .....	38
3.1.2. Numerical methods.....	40
3.2. Optical modelling of single-junction solar cells.....	43
3.2.1. Light absorption in nanowire arrays.....	43
3.2.2. Optical generation .....	46
3.2.3. Optical reciprocity and the Shockley-Queisser limit.....	48
3.3. Optical modelling of tandem solar cells.....	52
4. Electrical modelling.....	61
4.1. Electrical modelling at zero bias .....	61
4.2. I-V modelling in the 1D and 3D models .....	69
5. Light emission and photon recycling.....	75
5.1. Dyadic Green's functions and power flow .....	76
5.2. Numerical solution of Green's dyads in a periodic nanostructure .....	78
6. Conclusions and Outlook .....	81
References .....	83



# 1. General Introduction to Solar Cell Concepts

Over the past 15 years, global solar energy harvesting has increased by more than two orders of magnitude, as can be seen in Figure 1 [1]. In 2015, solar electrical power generation accounted for more than 1% of the total electrical power generation in the world. Solar energy harvesting, which is based mainly on the concept of solar cells, plays an essential role in both energy generation and daily life.

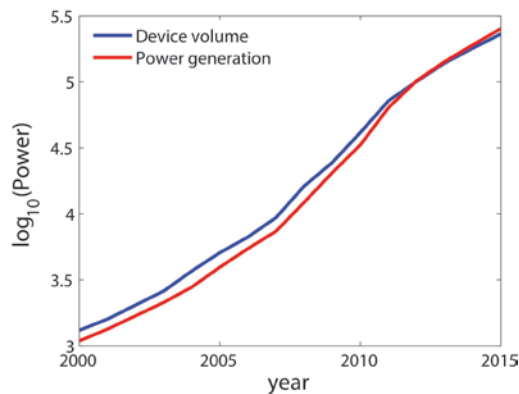


**Figure 1.** Global solar energy harvesting in the past 15 years. Data from the oil company BP [1]. Device volume describes the cumulative power generation capacity of solar cells (MW). Power generation is the actual solar power generated from solar cells in 2016 (GWh).

## 1.1. Solar spectra and solar power

As the importance of solar power increases, solar cells of various types have attracted a great deal of interest among researchers. To compare the energy-conversion efficiency of solar cells from different research teams, a standard solar energy spectrum must first be defined.

Standard reference spectra are known as air mass (AM) spectra, and are classified according to the height above the earth at which sunlight arrives (see Figure 2a). For example, sunlight in the outer atmosphere is defined as AM0, and the total input power is  $1348 \text{ W/m}^2$ .

In real applications, the spectrum used is usually AM1.5G or AM1.5D, which correspond to a zenith angle of  $48^\circ$  and a tilted surface of  $37^\circ$ , with total incident powers of  $1000 \text{ W/m}^2$  and  $900 \text{ W/m}^2$ , respectively [5]. In direct spectra (AM1.5D), only direct sunlight at AM1.5 is considered, while AM1.5G takes both direct sunlight and light scattered by the atmosphere into account.

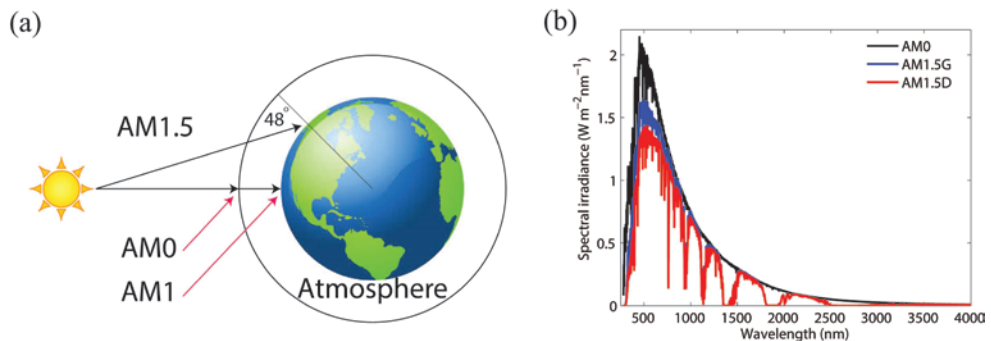


**Figure 2.** (a) Schematic drawing to illustrate the definition of the solar spectrum of AM0 AM1 and AM1.5. AM1.5 is measured by a surface tilt of  $37^\circ$ . (b) Solar spectrum for AM0, AM1.5D and AM1.5G from ASTM G173-03 reference spectra [2-4].

## 1.2. Absorption of light in semiconductors

Semiconductor p-n junction solar cells are one of the most important kinds of solar cells. A general introduction to semiconductor band structure theory and light absorption in semiconductors is given below.

The density of atoms in semiconductor lattices is quite high. For example, there are  $3.96 \times 10^{22}$  atoms in  $1 \text{ cm}^3$  of InP. The complex interaction between electrons and atomic nuclei makes it practically impossible to provide a strict solution to the Schrödinger equation due to the Coulomb interaction terms in the Hamiltonian. In solid state theory, this problem is usually solved by making a number of assumptions.

- a) The mass of the nucleus is usually 3 orders heavier than that of an electron. The position of the atomic core changes more slowly and to a lesser degree than the position of the electrons. It is assumed that the position of the atomic core is fixed when solving the equations for electron motion.
- b) A periodic potential is used instead of potential from separate atomic cores.
- c) The electrons are considered to be nearly-free electrons.

In some extreme cases, such as strongly correlated systems, the electron-electron interaction is comparable to the lattice-electron interaction. In this case, electron-electron interactions dominate. But for III-V bulk semiconductors and nanowires with diameters larger than a ‘truly’ one dimensional wire (typically less than a few nm in diameter), these approximations are usually valid.

When these approximations are applied, the Hamiltonian contains only two terms: the electron’s kinetic energy and its potential energy, which results in a single electron in a periodic potential:



$$[-\frac{\hbar^2}{2m^*}\nabla^2 + V(\vec{r})]\varphi = E\varphi \quad (1)$$

$$V(\vec{r}) = V(\vec{r} + \vec{R}) \quad (2)$$

where  $\vec{R}$  denotes the lattice period vector. This Hamiltonian can be solved using the pseudopotential method. Other models such as the tight-binding model and  $k \cdot p$  theory can also be used to calculate the band structure of a semiconductor.

In semiconductors, the electron states in a periodic lattice are split into separate energy bands. At a temperature of zero Kelvin, low-energy bands are filled with electrons, while high-energy bands are empty. The filled bands are referred to as valence bands, while the empty ones are called conduction bands. The energy difference between the bottom of the lowest-lying conduction band and the top of the highest-lying valence band is called the semiconductor bandgap.

Figure 3 illustrates typical single-photon absorption. An electron in the valence band absorbs one photon and is excited into the conduction band. This can only take place when the photon energy is greater than the bandgap. The resulting empty state in the valence band is usually denoted as a new type of charge carrier, a so-called ‘hole’. Excited electrons relax to the bottom of the conduction band and release heat, for example, due to electron-phonon scattering. The absorption of photons leads to an increasing number of free carriers (electrons in the conduction band and holes in the valence band) in the semiconductor, compared to a semiconductor in thermal equilibrium.

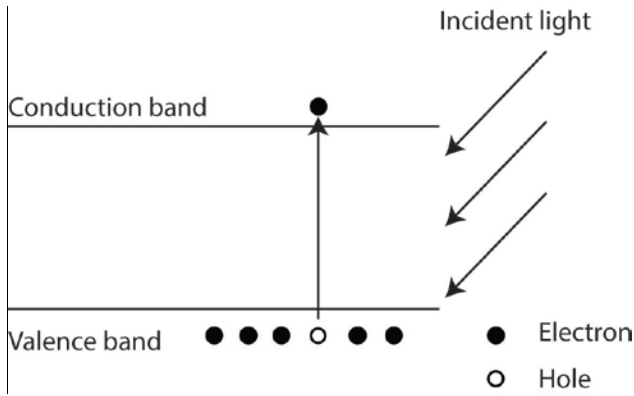


**Figure 3.** Light absorption in a semiconductor lattice.

In order to optimize the efficiency of a solar cell, as much of the incident light as possible should be absorbed by the active material. Many types of solar cells are based on free electron–hole pair generation, as described above.

### 1.3. Extraction of photogenerated charge carriers

The incident light, or solar energy, is transferred to the device material by optical absorption. Different types of solar cells exploit different ways of extracting photogenerated carriers (as discussed in Section 1.5). Here, p-n junction solar cells are used as an example of how carriers are split by the potential resulting from semiconductor doping.

It is possible to introduce additional charge carriers by adding dopants to intrinsic semiconductors. A dopant forms an impurity in the lattice, and introduces an impurity level inside the semiconductor bandgap. When the impurity level is close to the edge of the conduction band, the electron ionizes to the band. This type of doping leads to an n-doped semiconductor. When the impurity level is close to the edge of the valence band, it introduces additional holes, and forms a p-type semiconductor. Combining n- and p-type structures in the same lattice leads

to a space charge region between them. The band structure of the p-n junction is shown in Figure 4. An electrical field is intrinsically generated across the space charge region, which can help to separate, i.e., harvest, the solar-generated electron–hole pairs.

When a p-n junction is illuminated, optically generated electrons and holes are swept by the electric field towards different sides of the p-n junction, leading to an electric current at zero bias. A p-i-n junction can be formed by adding an intrinsic layer between the p and n segments, which increases the size of the depletion region, which has a high electron–hole splitting efficiency.

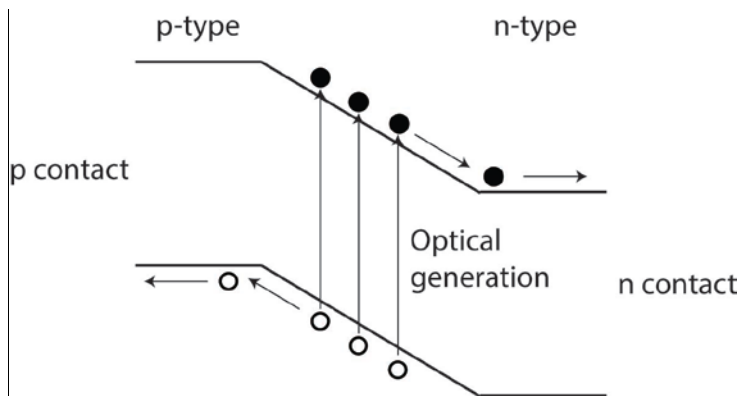


**Figure 4.** Carrier splitting in a semiconductor p-n junction.

## 1.4. Energy harvesting with a solar cell, and I-V response

The energy output of a solar cell can be calculated as the product of the photocurrent ( $I$ ) and the output voltage ( $V$ ).

$$P = IV \quad (3)$$

Figure 5 shows a typical I-V response of a p-n junction solar cell, with and without solar illumination. The photogenerated current at zero voltage is defined as the short-circuit current ( $J_{sc}$ ), while the voltage at zero current is defined as the open-circuit voltage ( $V_{oc}$ ), as indicated by the arrows. The area enclosed by the dashed red line in the top left corner gives the power density at a given voltage. The fill factor of solar cells is based on the total energy extraction, and is defined as the ratio between the highest total energy that can be extracted and the product of  $J_{sc}$  and  $V_{oc}$ .

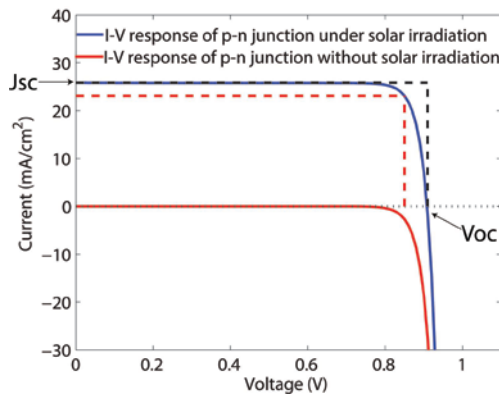


**Figure 5.** An example of the I-V response of a p-n junction solar cell with and without solar irradiation.

Another important property of a p-n junction solar cell is the ‘dark I-V’ or dark current [5, 6]. This is indicated by the solid red line in Figure 5. The dark current is a standard p-n junction I-V curve, which yields the intrinsic property of the p-n junction. It is a useful tool for analysing the behaviour of solar cells.

## 1.5. Different types of solar cells

In the previous section, the p-n junction solar cell was used as an example. This section provides a general introduction to other types of solar cells. The following

sections deal with nanowire array p-i-n junction solar cells, which are the primary focus of this thesis. Solar cells can be roughly categorized by concept, material or structure.

### **1.5.1. Categorization by concept**

The photovoltaic effect was first described in 1873 by H. N. Draper in selenium [7]. In 1883, Charles Fritts made the first solar cell using a selenium-gold Schottky junction, with an energy conversion efficiency of about 1%. The development of semiconductor band structure theory during the twentieth century promoted advancements in semiconductor technology and device design. Semiconductor p-n junctions were initially studied theoretically [8-10]. These studies yielded the famous S-Q limit, which is the maximum theoretical efficiency of a p-n junction solar cell [8] based on fundamental radiative recombination and the principle of optical reciprocity [11, 12]. This maximum efficiency is described as the balance between absorption and radiation in p-n junctions, and is a function of the semiconductor bandgap. It is assumed that the absorption of photons is perfect for all photons with energies greater than the bandgap. More technical details concerning the S-Q limit will be discussed in Chapter 3. Here, the conventional 1-sun S-Q limit for single p-n junction solar cells is discussed (Figure 6).

With a mirror substrate, with a reflectance,  $R$ , of 100%, radiation impinging on the substrate will be reflected back to the solar cell and re-absorbed without optical loss. When a semiconductor substrate is at the bottom, radiation is lost to the substrate, and will leak out of the solar cell, lowering the efficiency. In Figure 6, two peaks are visible around the bandgap of silicon and InP. These originate from the AM solar spectrum, which has sharp dips in several narrow photon energy ranges due to atmospheric absorption (see Figure 2b). The maximum efficiency, of 33.7%, is seen at the bandgap of InP (1.34 eV). Silicon and GaAs are also good solar cell materials, with efficiencies of 33.4% and 33.2% under the AM1.5G solar

spectrum. A substrate with refractive index  $n = 3.5$  has a 2-3% lower efficiency in the S-Q limit than a mirror with  $R = 100\%$ .

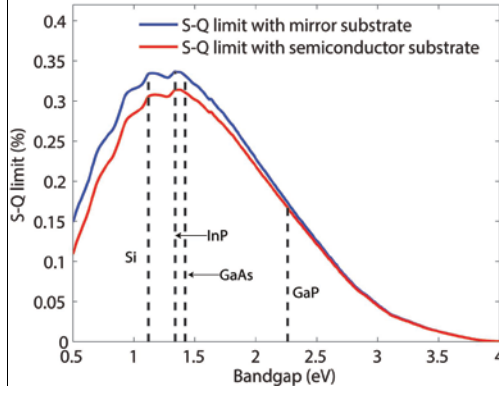


**Figure 6.** S-Q efficiency limit for a single p-n junction solar cell under the AM1.5G solar spectrum. The vertical dashed lines indicate the bandgaps of the respective materials.

The S-Q limit is calculated based on optical concepts such as absorption and radiation. However, solar cells can be characterized with concepts from semiconductor physics, where optically generated electron-hole pairs relax to their respective band edges, on average, to the quasi-Fermi level of electrons and holes.

Suppressing this thermal relaxation loss leads to a higher efficiency limit than the single-junction S-Q limit, when the same amount of photons is absorbed in solar cells. One direct way to reach this goal is to use a tandem solar cell with materials with different bandgaps.

Figure 7 (a) shows a schematic of a tandem p-n junction solar cell. The high-bandgap subcell is placed on top, and is denoted Cell 1 in Figures 7a and b. High-energy photons are absorbed in the top cell, while low-energy photons are transmitted to the second subcell. The thermal relaxation loss depends on the energy difference between the energy of photons and energy of bandgap. The tandem design reduces the overall thermal relaxation loss, as shown in Figure 7b, as only a

small fraction of the higher-energy photons reach the lower subcell. According to theoretical studies, the efficiency limit is a function of the number of cells [8]. The efficiency limit may be as high as 68% under one sun illumination for an infinite number of p-n junctions or subcells, and 86% under the highest concentration [10, 13]. However, in reality, more junctions lead to a higher complexity in device fabrication and an increasing amount of parasitic losses. At the end of 2016, 4-junction III-V tandem solar cells had the highest efficiency, 46% (under concentrated sunlight) [14].

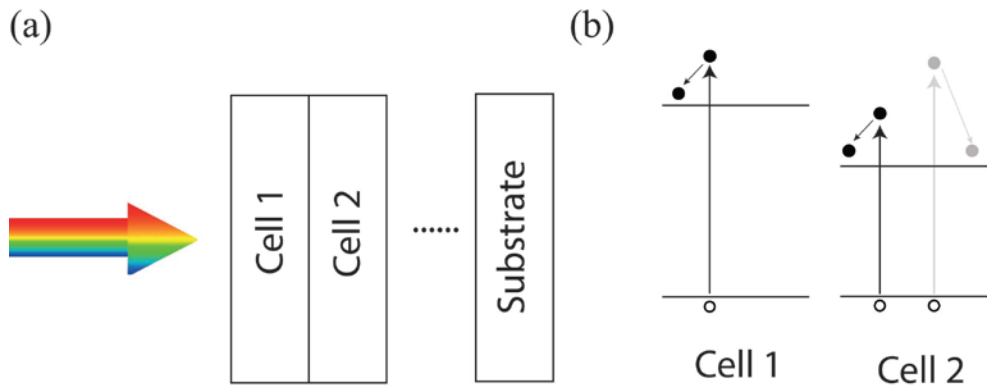


**Figure 7.** (a) Schematic of a tandem solar cell. (b) Thermal relaxation in different subcells. The grey channel in Cell 2 shows the absorption of a high-energy photon in a single-junction cell. This channel is suppressed in multi-junction cells as high-energy photons are absorbed predominantly in Cell 1.

The efficiency limit also depends on how the subcells are connected electrically. If they are connected in series, current matching is a strict requirement that should be carefully considered [Paper I]. Separate contacts for each cell provide a higher efficiency limit due to relaxation of the current-matching requirement [15]. The drawback of separately connected cells is that more output cables and more external electronics are required than when cells connected in series.

New concepts have also been developed to reduce thermal relaxation loss in solar cells. One of these is the hot-carrier solar cell, which harvests energy using electron and hole energy filters, before the thermal relaxation process sets in [16–20]. Theoretical studies have shown that the efficiency limit of hot-carrier solar cells could be as high as 66% under one solar AM1.5G spectrum [21]. However, it appears to be difficult in practice to extract electron–hole pairs before they relax. Fundamental studies of hot-carrier generation and thermal relaxation in nanostructures have recently attracted scientific interest [22, 23], although an experimental breakthrough has yet to be made in efficiency.

Another concept known as the intermediate-band solar cell (IBSC) is also a candidate for improving efficiency. This is based on the generation of an intermediate band in the bandgap of semiconductors. Three channels can then be used for light absorption: 1. between the conduction and valence bands, 2. between the conduction and intermediate bands, and 3. between the valence and intermediate bands. Theoretical studies have shown that the efficiency limit of the IBSC under one sun illumination is between that of 2 and 3 p-n junctions in the tandem cell [24]. A quantum dot superlattice has been used to generate this intermediate band experimentally [25, 26]. Nanowires with multiple quantum wells are also candidates for IBSCs, however, no reports have yet been published on high-efficiency nanowire multiple-quantum-well IBSCs.

Besides reducing thermal relaxation losses in solar cells, another approach to attain efficiencies beyond the single-junction S–Q limit is to use an ‘alternative sun’, i.e., to change the solar spectrum before or after it enters the cell, in order to achieve better spectrum matching. The conversion of light from low to high energy is known as photon up-conversion [27, 28], and correspondingly, high to low energy conversion is known as photon down-conversion [29]. Although an energy conversion efficiency of 100% is impossible, even in theory due to the second law of thermodynamics, this is still an interesting way of enhancing solar



cell efficiency. Recent experimental down-conversion of photon-to-photon quantum efficiency has been demonstrated with an efficiency above 100% [30]. The main challenge lies in applying this technique to photovoltaics. For up-conversion, it is still difficult to make an efficient up-converter [13], despite the predicted theoretical efficiency for a single junction solar cell of 44% under non-concentrated sunlight [31].

It is also difficult to make a device that can convert broadband sunlight into a spectrum suitable for a solar cell. An alternative to up- and down-conversion is thermal photovoltaics (TPV), in which an absorber is placed in front of the solar cell. Sunlight or other energy sources are used to heat the absorber, which then emits energy towards the solar cell. A photonic crystal with an optical band structure [32] is used to modify the radiation spectrum of the emitter. This technique modifies the light emission spectrum so that it is better matched to the solar cell. The theoretical efficiency limit of TPV has been reported to be up to 85.4%, while experimentally, an efficiency of only 23.6% has been reported [13, 33]. However, the low efficiency of energy transfer before the solar cell is still a serious problem in TPV.

The most widely used spectrum transformation method is solar-spectrum concentration. This can also be regarded as a special form of solar spectrum transformation before the solar cell. Higher concentration leads to a higher S–Q limit [8]. The maximum concentration that can be achieved in theory is 46200 times the normal one-sun illumination, which may increase the efficiency limit by 10% in absolute terms compared with single p-n junction solar cells [10]. One promising result reported so far is that the highest value of solar cell efficiency can be achieved by 4-junction III-V solar cells under 508-sun concentration [14]. However, concentration solar cells also have limitations. Only direct sunlight in the solar spectrum can be concentrated. Thus, most of the diffuse light in the atmosphere will not reach the cell. The amount of diffuse light can be estimated

from the difference between AM1.5G and AM1.5D, giving a value of about 100 W/m<sup>2</sup>, i.e., 10% of the total input power in AM1.5G.

Besides the time-symmetric systems discussed above, a new concept of time-asymmetric systems has been discussed by M. Green [13, 34]. The traditional S–Q limit is based on a time-symmetric system such that the light path is reversible. The absorptance of the system is equal to the emissivity at equilibrium. In time-asymmetric systems, the absorptance is not necessarily equal to the emissivity for reciprocal incident and outgoing angles. Thus, the fundamental light emission from a p-n junction can be suppressed, leading to an efficiency higher than the S–Q limit. A detailed study has shown that the energy conservation law excludes the possibility of totally suppressing the light emission [34]. Although the light emitted at angles within the incidence cone is reduced, the emission increases at other angles. By aligning the solar cells in the panel appropriately, the light emitted by one solar cell may be used by neighbouring cells, enhancing the solar cell efficiency up to an absolute value of 92.8% at ambient temperature (25 °C) [13, 35].

### **1.5.2. Categorization by material**

Silicon is a cheap material with a bandgap of 1.12 eV, which is suitable for single p-n junction solar cells, as shown in Figure 6. Experimental efficiencies of 25.0% had been achieved by 1998 [36], and this remained the highest value for silicon-based solar cells for the next 15 years. This record was broken by a slightly higher value of 25.6% in 2014 [37], and a value of 26.3% was achieved in 2016 by the use of a rear junction [14]. The S–Q limit of a single-junction silicon cell is 33.3%. When the Auger recombination of free carriers under solar illumination was included, this efficiency limit was calculated to be 29.4% with an optimized cell thickness of 110 µm [38, 39]. Experimental silicon solar cell efficiency is now approaching its theoretical limit in research laboratories [40]. Further

improvements in efficiency require accurate numerical simulations of light trapping and electron–hole recombination in semiconductors.

As silicon is an indirect-bandgap semiconductor with weaker absorption than a direct-bandgap semiconductor, the thickness of silicon solar cells is usually required to be one hundred to several hundred  $\mu\text{m}$  to obtain sufficient absorption of sunlight. Thick cells lead to a long diffusion path for the photogenerated electrons and holes in the semiconductor, increasing the probability of recombination compared with thin cells. It also increases the cost of the cell. Thin-film cells have a lower cost, but their efficiency is usually also lower than that of thick cells. The most efficient thin-film silicon cell produced to date, with a thickness of 1  $\mu\text{m}$ , has an efficiency of 11.4% [41], which is less than half that of a bulk cell.

Thinner cells can be made using a III-V semiconductor with a suitable, direct bandgap together with thin-film technology. The single p-n junction cell with the highest efficiency under one sun illumination (28.8%) is currently a GaAs thin-film cell with a thickness of about 2  $\mu\text{m}$  [14, 42]. Another advantage of III-V materials is that they can cover a large bandgap region from 0.2 eV to above 2 eV using ternary and quaternary compounds. This provides access to the best bandgap combination for a tandem solar cell. For example, the best bandgap combination (1.63 eV/0.96 eV) in a double p-n junction solar cell can be achieved with  $\text{GaIn}_{1-x}\text{P}_x$  and  $\text{InAs}_{1-y}\text{P}_y$  by simply changing the material composition  $x$  and  $y$ . However, III-V semiconductors suffer from considerable drawbacks. The cost of materials is quite high, and III-V semiconductor solar cells are currently mainly used in aerospace applications.

In parallel with silicon and III-V materials,  $\text{CdTe}$  and  $\text{CuIn}_x\text{Ga}_{1-x}\text{Se}_2$  (CIGS) are also good candidates for thin-film p-n junction solar cells. These, together with thin-film silicon solar cells dominate the thin-film market;  $\text{CdTe}$  cells having the largest share, and 21.5% being the highest reported efficiency [14, 38]. On the other hand, CIGS has a high absorption coefficient,  $>10^5 \text{ cm}^{-1}$ , for photons of

energies of 1.5 eV and above. This is about 100 times that for single crystalline silicon [43] at 1.5 eV. The best efficiency, of 21.7%, has been obtained for CIGS solar cells under 1 sun illumination [38].

Another promising type of solar cell is the dye-sensitized solar cell (DSSC), also known as the Grätzel cell [44]. The working principle is similar to photosynthesis. The most important advantage of DSSCs is that they do not require an elaborate manufacturing set-up. The highest reported efficiency for DSSCs is 11.9% [38, 45], which is still relatively low compared with other materials. DSSCs contain a liquid electrode, which is unstable under some conditions.

To overcome this shortcoming, materials with a perovskite crystalline structure have been used to make solid versions of DSSCs. Both organic and inorganic perovskites are the subject of a great deal of research due to their high efficiency and low cost [5, 46-53]. The highest reported efficiency for a perovskite-based solar cell is 21.0% [38]. However, perovskite solar cells have a smaller market share due to stability problems. The most stable device has been reported to retain about 90% of its efficiency over 60 days of operation [46]. Another promising type of perovskite solar cell is that utilizing the (anti)ferroelectric property to obtain values of  $V_{oc}$  higher than the bandgap. The material is usually an inorganic semiconductor with a perovskite lattice structure [54-56]. A  $V_{oc}$  of 120 V has been reported under one sun illumination using antiferroelectrics [56]. An efficiency above the S-Q limit at the corresponding bandgap has been reported using a ferroelectric insulator with an external quantum efficiency greater than 1 [55].

Other types of organic materials, such as polymers, could also be used in solar cell applications. Upon the absorption of light in the material, electrons will be excited from the highest occupied molecular orbital state to the lowest unoccupied molecular orbital, forming an exciton. The electrodes split the exciton and solar cell harvests the energy. The highest reported efficiency of this kind of organic cell is 11.2% [57] under one sun illumination.

### 1.5.3. Categorization by structure

In addition to materials, structure is also an important feature of solar cells. A planar surface with a refractive index of about 3.5 is typical for III-V materials. The reflection of normally incident light at the air–semiconductor interface can be as high as 31%. One or multiple layers of anti-reflection coating (ARC) could reduce the reflection significantly [58]. Introducing a nano- or micro-scale surface texture on the front of thick silicon solar cells could increase the path length of light in the silicon, and thus reduce the reflection at the interface. As absorption is proportional to the path length, according to the Beer–Lambert law, it is possible to make a thinner silicon cell with good sunlight absorption properties while reducing the cost of the material.

Quantum dots are another possible nanostructure for solar cells. The best reported efficiency of a colloid quantum dot solar cell is 9.9% [38]. This applies to a pure quantum dot solar cell. There are other ways of using quantum dots as part of the active layer. For instance, a quantum dot superlattice can be made in a GaAs p-n junction to generate an IBSC [26].

Making the p-n junction directly in the nanostructure could also enhance light absorption and reduce the cost of material. For example, a vertical nanowire array is a good candidate for a large-array, single-junction or tandem solar cell device [59, 60]. III-V nanowire-array p-n junction solar cells were the subject studied in this work, and will be described in more detail in the following chapters.

## 2. III-V Nanowire Array Solar Cells

Developments in recent years have made it possible to fabricate nanowire photo-detectors [61, 62], nanowire light-emitting diodes [63, 64], nanowire lasers [65, 66] and nanowire solar cells [59, 60, 67, 68]. Two designs of nanowire solar cells are usually considered: axial and radial junctions, as shown in Figure 8.

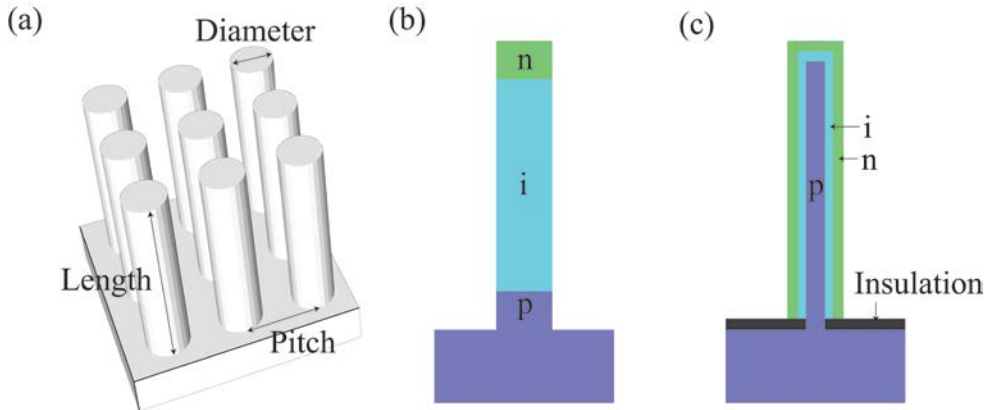


**Figure 8.** Schematic illustrations of: (a) a nanowire array, (b) one unit cell of an axial NWASC, (c) one unit cell of a radial p-i-n junction nanowire solar cell.

An efficiency of 15.3% has been achieved using a  $2.8\ \mu\text{m}$  long axial p-i-n junction GaAs nanowire array, with the nanowires covering only 13% of the surface area [67]. The best experimental efficiency for a GaAs nanowire array using a radial p-i-n junction reported to date is 7.4% [68]. This is lower than the axial junction efficiency, although modelling has shown that the reduction in current with increasing surface recombination velocity can be lower in radial junction solar cells than in axial junction cells [69, 70]. InP single-junction nanowire array cells

fabricated using the top-down etching technique have been reported to have an efficiency of 17.8% [71]. In addition to these studies on single-junction arrays, an experimental efficiency of 11.4% and voltage addition have recently been achieved in a tandem configuration with a GaAs nanowire array cell on a silicon substrate p-n junction [60].

## 2.1. Merits of nanowire arrays in solar cell applications

### 2.1.1. More freedom in lattice matching

Lattice matching between different materials is a significant limitation of planar III-V tandem solar cells. The only lattice-matched case for GaInP/GaAs dual-junction planar cells is  $\text{Ga}_{0.5}\text{In}_{0.5}\text{P}$  on GaAs, as other compositions of  $\text{Ga}_x\text{In}_{1-x}\text{P}$  with different bandgaps lead to poor crystal quality at the interface, which leads to recombination centres that degrade the electrical characteristics of the cell. However, the development of wafer bonding techniques in recent years [72] has relaxed the requirements on lattice matching, through the use of two substrates during growth and bonding them to produce tandem cells. Lattice matching between each substrate and the active layer is still a limitation, and for some materials, such as InSb, there is no suitable growth substrate due to its large lattice constant. However, small platelets of high-quality InSb [73] or clusters of InSb nanowire arrays [Paper IV] could be grown on either a silicon or InAs substrate using a short nanowire segment as a transition layer. The lattice mismatch tolerance makes nanowire solar cells more flexible at the material selection stage, especially in the case of tandem cells [Paper I].

### **2.1.2. Enhanced absorption and cost-effectiveness**

For the standing nanowire array illustrated in Figure 8a, light incident on top of the array couples into the nanowire, rather than being reflected back, in contrast to a planar structure. The reduction in reflection and strong photon confinement in a nanowire array lead to broadband absorption enhancement. Nanowire arrays thus offer the possibility of achieving high-efficiency solar cell devices requiring less material. A 20 times stronger absorption per unit volume of material than in a bulk semiconductor has been reported by parameter tuning of nanowire arrays [74]. In contrast, only the thickness can be tuned in thin-film cells in the design of the active solar cell layer. Nanowire arrays thus provide extra dimensions for the design and optimization of photovoltaics devices. The amount of material required in a NWASC is only 20% of that required in thin-film cells with bulk-like photocurrent [14, 67], which will reduce the cost of fabricating the active layer.

Due to the tolerance in lattice mismatch, nanowire arrays can be grown directly on an inexpensive substrate such as silicon [60, 75]. Recently developed peel-off technology may also contribute to minimizing the cost of the substrate [76]. It is possible to peel the nanowire array off III-V substrates and then reuse the substrates for further growth. Another growth method known as aerotaxy [77] involves growing the nanowires in a gas flow instead of on a substrate. These methods could potentially reduce the cost of manufacturing III-V materials for photovoltaics.

## **2.2. Nanowire array solar cell designs**

Two kinds of design can be used for NWASCs. One is known as the axial p-i-n junction (Figure 8b). The n, p doped and intrinsic segments are stacked in layers from top to bottom, as in thin-film or bulk solar cells. One way of fabricating axial



junction nanowire solar cells is by particle-assisted nanowire growth. In this method, catalyst particles, for example, of Au, are deposited on the substrate in the desired pattern. This is then placed in a chamber containing chemical gas. The gas particles enter the liquid catalyst particle and end in a solid phase nanowire. This is known as vapour-liquid-solid epitaxy [78]. An inert mask with periodic holes can be used to define the position where epitaxial growth is to take place.  $\text{Si}_3\text{N}_4$  is one candidate for such a mask [Paper III]. In this way, regular nanowire arrays with a fixed pitch (separation) can be grown over a large area. The nanowires can be doped during growth by adding the appropriate gas, and p-n junctions can be created in the nanowire.

Compared to p-n junctions, the p-i-n junction has a larger depletion region in which the electric field is strong. This results in a greatly improved electron-hole splitting efficiency in materials with a short diffusion length [Paper II]. This can be verified by electron-beam-induced current (EBIC) measurements [67]. The electron-hole splitting efficiency is high in the intrinsic region. From this point of view, a larger intrinsic region can lead to a higher photogenerated current in the solar cell.

Axial junction nanowire solar cells are sensitive to surface effects, especially in the intrinsic region. The excess carrier concentration is relatively high in the intrinsic region under a certain bias, due to quasi-Fermi level splitting. Excess electrons and holes have a higher probability of recombining at surface traps in a long intrinsic region, which limits the open-circuit voltage. One possible solution is to use a high-bandgap material as a surface coating to passivate the nanowire [67]. This can reduce the surface recombination velocity by several orders of magnitude, especially for GaAs nanowires, which have a high surface recombination velocity, up to  $10^7$  cm/s for an unpassivated surface [79].

An alternative to surface passivation is to use a core-shell structure or a radial p-i-n structure, as shown in Figure 8c. In such a structure, the intrinsic part of the

nanowire is not at the surface, and the surface may be far away from the excess carriers, possibly providing better tolerance to surface recombination [69, 70].

With regard to fabrication, a radial junction can be created by radial shell growth on a nanowire core. A more complicated junction shape, combining the characteristics of a radial and an axial junction, has recently been achieved, and a solar cell efficiency of about 5% was reported with this structure [80].

In parallel with the standing nanowire array, the single lateral nanowire is an interesting device design for both theoretical and experimental studies [11, 80]. Enhancement of the open-circuit voltage has been predicted by theoretical calculations [11], while the enhancement of absorption has been observed in experiments comparing vertical and lateral nanowire solar cells [80]. Despite these advantages, difficulties are still encountered in making large-area lateral nanowire solar cell devices.



### 3. Optical modelling of nanowire array solar cells

When modelling NWASCs, light scattering in the nanostructure must be taken into consideration first. In principle, all light scattering problems can be described as a solution to the Maxwell equations, except for quantum optics. Various assumptions are applied, depending on the size of the structures, to simplify the numerical or analytical solutions.

a) **Structures much larger than the wavelength of light**

The light is described by ray optics, which means that it can be treated as a beam. The solution can be found by ray tracing.

b) **Structures smaller than or similar to the wavelength of light** (Typically  $10^{-8}$  to  $10^{-6}$  m in the visible wavelength range.)

The light is described by a solution to the conventional Maxwell equations. Light is regarded as being in the form of a wave instead of a ray [81].

c) **Structures  $10^{-14}$  to  $10^{-10}$  m, time period in the range  $10^{-17}$  to  $10^{-13}$  s**

The light is described by a solution to the microscopic Maxwell equations. Light is regarded as being in the form of a wave. A time-averaged solution is necessary to yield a smooth electrical and magnetic field. In some extreme cases, such as quantum optics or extremely strong field optics, Maxwell's equations may fail. Quantum electrodynamics should then be applied instead.

In nanowire solar cell modelling, the size of the finest structure is usually 10-100 nm. A solution to Maxwell's equations should therefore provide a good description.

To simplify the solution process, we assume the electric and magnetic field to have a time harmonic form, and the material to have a linear and local response to electromagnetic fields. Maxwell's equations in the frequency domain can then be written as [82]:

$$\nabla \times \vec{E} = i\omega \tilde{\mu} \vec{H}, \nabla \times \vec{H} = -i\omega \tilde{\epsilon} \vec{E} \quad (4a)$$

$$\nabla \cdot (\tilde{\mu} \vec{H}) = 0, \nabla \cdot (\tilde{\epsilon} \vec{E}) = 0 \quad (4b)$$

$$\vec{D} = \tilde{\epsilon} \vec{E} = \tilde{\epsilon} \vec{E}_0 e^{-i\omega t}, \vec{B} = \tilde{\mu} \vec{H} = \tilde{\mu} \vec{H}_0 e^{-i\omega t} \quad (4c)$$

where  $\omega$  is the frequency of light,  $\tilde{\epsilon} = \epsilon_0 \tilde{\epsilon}_r$  is the complex dielectric function and  $\tilde{\mu} = \mu_0 \tilde{\mu}_r$  is the complex magnetic permeability, which equals  $\mu_0$  for non-magnetic materials.  $\mu_0$  and  $\epsilon_0$  denote the vacuum permeability and vacuum permittivity, respectively. In these equations, the real electric and magnetic fields are extended to complex-valued fields for convenience (it is understood that the physical electric and magnetic fields correspond to the real parts of these fields).

## 3.1. Methods of solving Maxwell's equations

### 3.1.1. Optical properties of semiconductors

In Equation (4), optical properties of material are described by the phenomenological parameter  $\tilde{\epsilon}$ . This could be calculated, in principle, by framework theory. Interband light absorption can be described as the transition of an electron from the filled state in the valence band to the empty state in the conduction band, as shown in Figure 3. The probability of transition is described by Fermi's golden

rule, and the absorptance of materials, as well as their optical parameters, can be calculated accordingly [83].

In reality, the precise calculation of the band structure is difficult. For example, first-principle calculations based on GW theory may yield a good description of the band structure at temperature of 0 K. Unfortunately, applications to room-temperature devices are beyond our current theoretical and computational ability. As a result, phenomenological theory is used instead of an exact theoretical framework. A complex-valued refractive index,  $\tilde{n} = \sqrt{\tilde{\epsilon}_r \tilde{\mu}_r} = n + ik$ , is used to describe the material's optical properties. The real part of the refractive index, that is,  $n$ , dominates light scattering and propagation when the imaginary part  $k$  is small. A non-zero imaginary part of the refractive index leads to absorption in the material. The light absorption in a planar material can be calculated in accordance with the Beer–Lambert law:

$$A(\lambda) = T(\lambda)[1 - \exp(-4\pi kL/\lambda)] \quad (5)$$

where  $A$  is the absorptance,  $T$  is the transmittance from medium of the incident light to the material,  $k$  is the imaginary part of the refractive index and  $L$  is the thickness. Back-scattering from the back of the device is not taken into consideration in this equation. The light absorption in planar structures can be calculated with this equation by inserting the refractive index from experiments or optical handbooks.

Apart from inter-band absorption, free-carrier absorption also plays a role in III-V semiconductor applications in the near infrared (IR) and visible light regions, especially for heavily doped semiconductors. The dielectric function of free-carrier absorption can be calculated using the Drude model [84]:

$$\tilde{\epsilon}(\omega) = \epsilon_s \left( 1 - \frac{\omega_p^2}{\omega^2 + i\omega\Gamma} \right), \quad \omega_p^2 = \frac{ne^2}{\epsilon_s \epsilon_0 m^*} \quad (6)$$

where  $\Gamma$  is the scattering rate, typically  $10^{-14}$  s,  $\omega$  is the frequency of light,  $\omega_p$  is the plasma frequency of doped material,  $n$  is the free-carrier concentration and  $\epsilon_s$  is the relative permittivity of the undoped semiconductor. Substituting  $\tilde{n} = \sqrt{\epsilon}$ , allows the refractive index to be calculated from Equation (6). This plasma refractive index changes the optical response of the intrinsic material around the plasma frequency,  $\omega_p$ , and in the lower frequency region. The plasma frequency typically corresponds to the IR region with a doping level of  $10^{18}$  to  $10^{19}$  cm<sup>-3</sup>. Free-carrier absorption is not usually beneficial in solar cell applications as the excited carriers relax quickly and release energy in the form of heat without contributing excess carriers to the photogenerated current. It leads to a narrow spectral region of total reflection known as the Reststrahlen band [84].

### 3.1.2. Numerical methods

It is often difficult to find an analytical solution to Maxwell's equations for nanostructures. Various numerical methods have been developed to study these systems. A brief introduction to the methods used in this work is given below.

#### a) Scattering matrix method

In this method, light propagation is described along one Cartesian direction. The system is divided into many slices along this direction. The dielectric function in each layer is invariant along the direction of light propagation. It is possible to solve for optical eigenmodes within each layer. These eigenmodes constitute a complete basis for forward- and backward-propagating light, and the light in each layer can therefore be expressed as a superposition of these modes. Light propagation in this system then transforms into finding the eigenmodes and expansion coefficients in each layer; and then matching the expansion coefficients between different layers. This is known as the Fourier modal method. With the introduction of scattering matrices into the

Fourier modal method, the incident light can be fixed as a natural boundary condition, as in experiments, and no exponentially growing eigenmodes appear explicitly in the solution, enhancing the numerical stability [82]. Note that this method is closely related to the rigorous coupled-wave analysis method [85].

b) Finite-element method

The finite-element method (FEM) provides a general way of solving partial differential equations. The method depends on the variational principle. A common way of using this method is summarized briefly below.

Firstly, the problem of solving differential equations with a boundary condition is transformed into the problem of minimizing a function. Secondly, the region is divided into a mesh consisting of elements. Thirdly, the FEM equation sets are constructed and modified with appropriate boundary conditions. Finally, the standard method for the solution of systems of linear equations is used to find a converging solution.

Various kinds of commercial FEM software are available. The program used in the present work as a FEM solver to investigate the properties of NWASCs was Comsol Multiphysics as a FEM solver to investigate the properties of NWASCs.

The numerical results obtained with the scattering matrix method and FEM agree very well (Figure 9). This is expected since they solve the same Maxwell equations under the same boundary conditions. Furthermore, such modelling tends to agree well with the results of experiments [86]. The numerical accuracy of modelling can be estimated roughly as the difference between these two methods, which is approximately 1% in the absolute values in Figure 9. Note that the accuracy could be increased by increasing the computational effort. The scattering matrix method takes less than 1 minute on a Dell laptop (Latitude 14 7000 Series



Ultrabook™ [E7440]) with an underlying Fourier basis with 5 harmonics in each of the two in-plane directions. To obtain similar accuracy with Comsol requires more than half an hour with the same computer, but Comsol is faster for calculating the electric field distribution. Therefore, it was considered more convenient to calculate the spectrum with the scattering matrix method and the field distribution with Comsol for selected wavelengths.

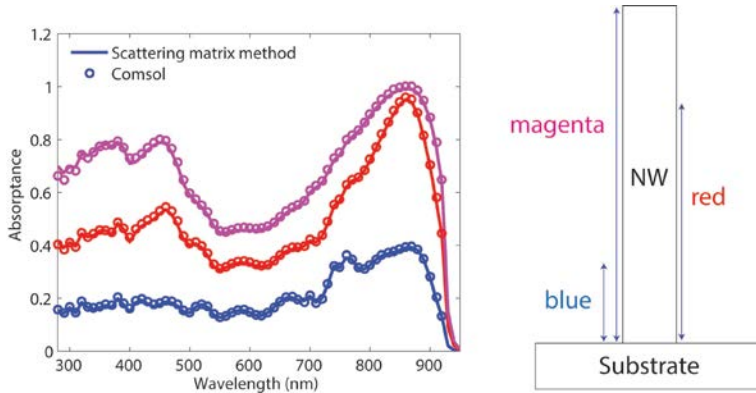


**Figure 9.** Absorbance of an InP nanowire array with a pitch of 700 nm, diameter of 180 nm and length of 2000 nm. The solid lines show the results obtained with the scattering matrix method, and the circles are the results obtained with Comsol. The magenta line shows the absorbance in the complete nanowire, the red line the absorbance in the bottom-most 1200 nm of the nanowire, and the blue line the bottom-most 400 nm. Note that the absorbance is defined as the fraction of incident light absorbed.

Both the scattering matrix method and Comsol work well for simple square and hexagonal nanowire arrays, as well as for more complex structures [Paper IV]. Comsol can produce high-quality colour images of electric fields and other plots, as shown in Figure 10.

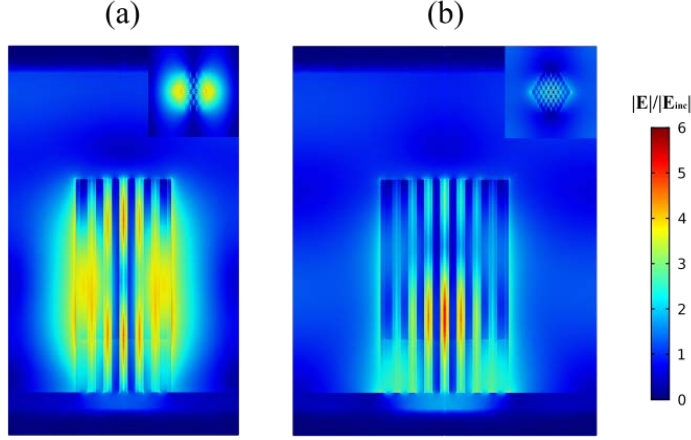


**Figure 10.** Electric field intensity for a fixed wavelength for an InSb nanowire cluster array [Paper IV]. The figure shows only 1 unit cell in side view, and the inset shows the top view. (a) Nanowire cluster into which incident light couples strongly. (b) Nanowire cluster into which incident light couples more weakly than in (a).

## 3.2. Optical modelling of single-junction solar cells

### 3.2.1. Light absorption in nanowire arrays

For material parameters such as the refractive index, tabulated bulk values from handbooks or research articles were used. Simulations using the bulk refractive index are usually in good agreement with experimental results [86].

An important optical response characteristic of a standing nanowire array as shown in Figure 8, is the dependence of the so-called  $HE_{1n}$  resonance on the nanowire diameter. The notation of the mode comes from fibre-optics. Such a ‘hybrid’ mode propagates along the axis of the fibre and has both an electric and a magnetic field component in the direction parallel to the axis, that is, in the propagation direction. A mode in which the electric field dominates is denoted a HE mode,

while a mode in which the magnetic field dominates is denoted an EH mode [87]. This is a strict eigenmode solution for a single nanowire or a fibre. Modes similar to those in a single wire or a fibre tend to appear in nanowire arrays, and the same notation is therefore used [88].

Resonances in the eigenmode can occur at specific wavelengths, resulting in the enhancement of the electric field in the nanowires and a peak in optical absorption. The resonance wavelength depends on the nanowire diameter. The absorption peak shifts to longer wavelengths with increasing nanowire diameter, and disappears at the bandgap. An example is shown for an InP nanowire array in Figure 11. The black arrows indicate the fundamental  $HE_{11}$  mode, which always exists in a nanowire array without a cut-off frequency. In these InP nanowires, the absorption peak is located close to the bandgap for a diameter of 180 nm, leading to current enhancement in single-junction and tandem solar cells [89] [Paper I]. Similarly for the  $HE_{1n}$  mode, the short-circuit current and efficiency of both types of solar cell are a maximum when the corresponding absorption peak is close to the nanowire bandgap, provided other geometrical parameters, such as the array pitch, are optimized [89] [Paper I]. The term ‘ $HE_{1n}$  eigenmode resonance’ is used to denote the maximum value of solar cell efficiency, and the  $HE_{11}$  eigenmode resonance usually yields the highest efficiency. The solar cell current enhancement diameter of the nanowire array can be predicted by the following equation:

$$D_{HE1n} n_{\text{bandgap}} E_{\text{bandgap}} = \text{constant}_{HE1n} \quad (7)$$

where  $D_{HE1n}$  is the resonance diameter,  $n_{\text{bandgap}}$  is the real part of the refractive index around the bandgap, and  $E_{\text{bandgap}}$  is the bandgap energy. The right-hand constant can be estimated from InP data in Ref. [89]. Inserting this value gives  $D_{HE11} = 180$  nm for  $n_{\text{bandgap}} = 3.5$  and  $E_{\text{bandgap}} = 1.34$  eV. This equation can be used to estimate the best diameter of the nanowire in either the single-junction or tandem design, provided the tandem cell does not require current matching between the subcells.  $HE_{11}$  is thus usually the best candidate for solar cell applications [Paper I,

III]. The  $HE_{12}$  mode yields the highest efficiency for a large-diameter nanowire, as indicated by the red arrow in Figure 11.

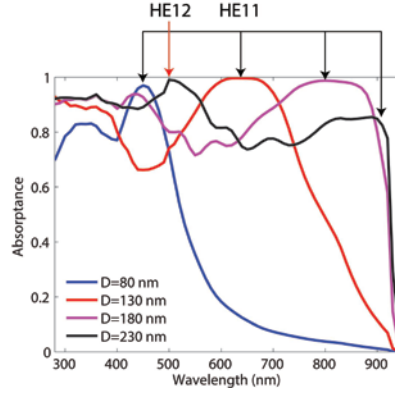


**Figure 11.** Absorbance of InP nanowire arrays with a pitch of 500 nm and length of 2000 nm. The black arrows indicate the positions of the  $HE_{11}$  absorption peak for nanowire arrays of varying diameter. Note that for wavelengths of incident light above 925 nm (the bandgap wavelength of InP) the absorbance falls rapidly due to the reduction in absorption of the InP material. The red arrow indicates the absorption peak for the  $HE_{12}$  resonance.

For a nanowire material such as InSb, which has a small bandgap, the diameter required for the  $HE_{11}$  resonance is more than 1  $\mu\text{m}$ . Such large diameters are associated with difficulties in growth and nanoprocessing [61]. One possible solution is to use a cluster of smaller-diameter nanowires instead of a single large-diameter wire, and to coat the smaller wires with a high-refractive-index coating such as  $\text{HfO}_2$ . Figure 10 shows nanowire clusters with strong and weak coupling to the incident light. In the case of strong coupling, there is considerable field enhancement around and within the nanowires in the cluster. This field enhancement leads to strong optical absorbance at this wavelength, similar to the  $HE_{11}$  resonance in single wires, while the absorbance is small in the weak coupling case. It is possible to make an IR photon detector with this kind of structure by tuning the nanowire geometry [Paper IV].

For tandem solar cells with more junctions, the bottom cell has a material with a lower bandgap and the optimum diameter of the nanowires is quite large. The same pitch and diameter may not be appropriate for both the top and bottom cell. A design with a nanowire cluster cell on top of a large-diameter nanowire bottom cell could improve the efficiency of the solar cell.

### 3.2.2. Optical generation

The overall absorption in nanowires is known from the absorptance spectrum. For opto-electronic analysis, it is important to know where photogeneration occurs spatially since the p-n junction design is expected to affect the electron–hole splitting efficiency [Paper II].

Considering the inter-band absorption, and assuming that each absorbed photon generates a single electron–hole pair, optical generation can be written as:

$$G(\vec{r}) = \int_{\lambda_{\text{start}}}^{\lambda_{\text{bandgap}}} \frac{A_e(\vec{r}, \lambda)}{E_{\text{photon}}} d\lambda \quad (8)$$

where  $G$  denotes the number of electron–hole pairs generated at position  $\vec{r}$ , and  $A_e$  is the absorbed energy density at position  $\vec{r}$  for incident light of wavelength  $\lambda$ . The wavelength is integrated from 280 nm, below which the solar spectrum has negligible intensity, to the wavelength corresponding to the bandgap of the semiconductor.

To arrive at optical generation, we need to calculate  $A_e$  at a fixed position for a single wavelength. Assuming a small volume and applying Gauss's theorem, the net energy flux into this small area equals the energy absorption of the area:

$$\iiint A_e(\vec{r}, \lambda) dV = \oint \vec{P} \cdot d\vec{S} = \iiint \nabla \cdot \vec{P} dV \quad (9)$$

where  $\vec{P}$  is the Poynting vector. As this equation holds true for an arbitrary closed surface, we have the differential form:

$$A_e(\vec{r}, \lambda) = \nabla \cdot \vec{P} = \frac{1}{2} \text{Re}(\nabla \cdot \vec{E} \times \vec{H}^*) = \frac{1}{2} \text{Re}[\vec{H}^* \cdot (\nabla \times \vec{E}) - \vec{E} \cdot (\nabla \times \vec{H}^*)]. \quad (10)$$

The above equation can be simplified by the Maxwell's equations:

$$A_e(\vec{r}, \lambda) = -\frac{1}{2} \text{Re}[\mu \vec{H}^* \cdot \frac{\partial \vec{B}}{\partial t} + \epsilon^* \vec{E} \cdot \frac{\partial \vec{D}^*}{\partial t}]. \quad (11)$$

Assuming, as for Equation (4), that the electromagnetic wave has the form  $\vec{H} = A \exp(i\omega t)$ ,  $E = B \exp(i\omega t)$ , then the above equation can be rewritten.

$$A_e(\vec{r}, \lambda) = -\frac{1}{2} \text{Re}[i\omega \mu \vec{H}^* \cdot \vec{B} + i\omega \epsilon^* \vec{E} \cdot \vec{D}^*]. \quad (12)$$

For non-magnetic material, the first term on the right-hand side equals zero, as  $\mu$  is a real number. Thus, inserting  $\epsilon = \epsilon_r \epsilon_0 = (n + ik)^2 \epsilon_0$  gives

$$A = -\frac{1}{2} \text{Re}[i\omega \vec{E} \cdot \vec{D}^*] = -\frac{1}{2} \text{Re}[i\omega \vec{E} \cdot \epsilon_0 (n + ik)^2 \vec{E}^*] = nk\omega \epsilon_0 |\vec{E}^2|. \quad (13)$$

Combining Equations (8) and (13), we arrive at the expression for optical generation rate:

$$G(\vec{r}) = \int_{\lambda_{\text{start}}}^{\lambda_{\text{bandgap}}} \frac{nk\epsilon_0 |\vec{E}^2|}{h} d\lambda. \quad (14)$$

An example of the optical generation of one unit cell in a standing nanowire array is shown in Figure 12.

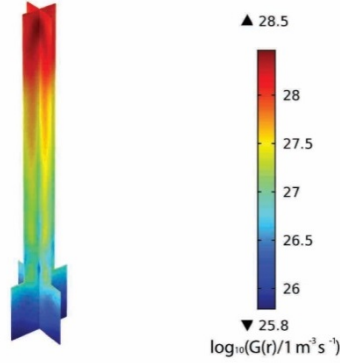


**Figure 12.** Optical generation in an InP nanowire array, with a nanowire diameter of 180 nm, pitch of 330 nm and length of 1400 nm. The geometry was optimized to give the maximum solar cell current for a 1400 nm long InP nanowire array. (Figure from Paper II.)

### 3.2.3. Optical reciprocity and the Shockley-Queisser limit

The efficiency of the working device depends on the balance between optical generation, recombination and charge extraction of the solar cell. Optical generation has been discussed in previous section. This section focuses on the fundamental optical loss, which is due to radiative recombination. The electrical losses from the surface of the contacts, Shockley–Read–Hall (SRH) recombination, and Auger recombination will be discussed in Chapter 4.

Two methods can be used to account for optical loss through light emission. One is through the use of optical reciprocity, and is based on the following assumptions [90, 91].

- a) Lorentz reciprocity can be applied to the emitter.
- b) The system is close enough to thermal equilibrium.

Under these assumptions, the following equation is obtained [92]:

$$A(\omega, \theta, \varphi) = e(\omega, \theta, \varphi) \quad (15)$$

where  $A(\omega, \theta, \varphi)$  is the directional spectral absorptivity and  $e(\omega, \theta, \varphi)$  is the directional emissivity, as shown in Figure 13. This is also known as directional Kirchhoff reciprocity [90]. At equilibrium, there is no net optical flux through any unit surface. For perfect black body, we have  $A(\omega, \theta, \varphi) = e(\omega, \theta, \varphi) = 1$ .

For a solar cell with perfect absorptance, the emissivity should also be unity. This maximum integrated emissivity indicates that the emissivity in any direction is equal to 1.

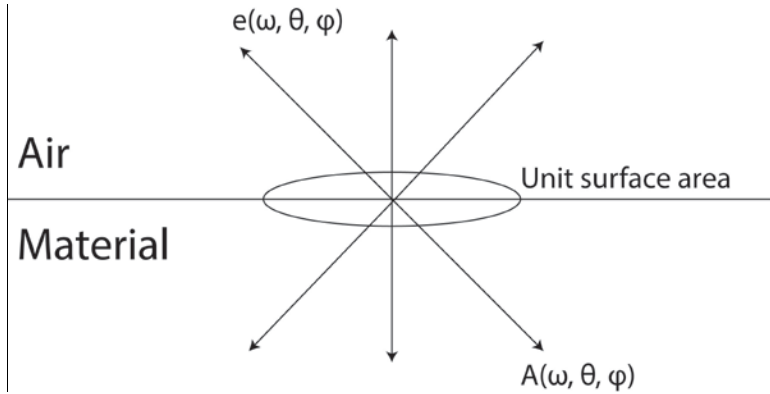


**Figure 13.** Schematic illustration of radiation from the surrounding air to a solar cell and solar cell emission to air at equilibrium.

The principle of optical reciprocity, together with perfect absorption, yields the famous S–Q limit for a p–n junction solar cell based on the following assumptions [8].

- a) Each photon with an energy greater than the bandgap generates one electron–hole pair.
- b) The intensity of the incident light is given by the solar spectrum.
- c) The solar cell emits as a black body with a wavelength cut-off at the bandgap.

Under assumptions a) and b), the solar current can be written:



$$j_{sc} = e \int_{\lambda_{start}}^{\lambda_{bandgap}} \frac{\lambda A(\omega, \theta, \varphi) I_{AM1.5}(\lambda)}{2\pi c \hbar} d\lambda \quad (16)$$

where  $c$  is the speed of light in vacuum and  $I_{AM1.5}$  denotes the AM1.5 solar spectrum.

Assumption c) allows the recombination to be written in the form of the Shockley diode equation:

$$j_{rec}(V) = e F_{c0} [\exp\left(\frac{eV}{k_b T}\right) - 1] \quad (17)$$

where  $k_b$  is the Boltzmann constant and  $F_{c0}$  is the recombination current at zero voltage, which can be regarded as the equilibrium state [11, 12, 93]:

$$F_{c0} = 2\pi \int_0^{2\pi} d\varphi \int_0^{\frac{\pi}{2}} d\theta \int_{\lambda_{start}}^{\lambda_{bandgap}} \theta(\lambda) A(\lambda, \theta, \varphi) \cos\theta \sin\theta d\lambda \quad (18)$$

$$\frac{\Omega(\omega)}{\hbar\omega} d\omega = \theta(\lambda) d\lambda = \frac{2cn^2}{\lambda^4 (\exp\left(\frac{2\pi c \hbar}{\lambda k_b T}\right) - 1)} d\lambda, A(\lambda, \theta, \varphi) = 1 \quad (19)$$

where  $\theta(\lambda)$  is the photon density flux of blackbody radiation at temperature  $T$ , and  $n$  is the refractive index of the material next to the solar cell. The optical reciprocity, that is, Equation (15), has already been applied. Radiation is assumed to be incident only on the top of the cell, as a perfect mirror, for example, with  $n = 0$ , was assumed on the back in order to reduce recombination, in the efficiency limit calculation. Combining Equations (16) and (19) gives the I-V response of the solar cell:

$$j = j_{sc} - j_{rec}(V). \quad (20)$$

The solar cell efficiency is calculated at the maximum value of  $P = jV$ . Assuming that  $A(\lambda, \theta, \varphi) = 1$ , a S-Q solar cell efficiency limit can be obtained as a function of the semiconductor bandgap, as shown in Figure 6. This limit is the best efficiency of a single p-n junction, time-symmetric solar cell under one sun illumination without limiting the range of radiative emission angles. Concentrating

the sunlight or limiting the range of radiative emission angles allows a higher efficiency, of up to about 45.2%, for a single p-n junction cell.

In the modelling of a nanowire array single-junction solar cell, the absorption spectrum was calculated with the scattering matrix method using normal incidence to obtain the short-circuit current. A set of spectra with various values of  $\theta$  and  $\varphi$  was then calculated to obtain the recombination current. A limit higher than the S–Q limit was found for a single p-n junction nanowire array on a substrate [93], originating from the intrinsic radiative emission angle limitation of the nanowire array.

The other way of considering light emission loss is the reverse process, as shown in Figure 3. Optically generated electron–hole pairs recombine and emit photons in the semiconductor. These photons are either once again absorbed in the semiconductor, or emitted to the surroundings. To model this radiation and reabsorption, one dipole must be placed at a position in the nanowire and the photon recycling from this dipole emission calculated. The dipole models the light emission at this fixed point. Changing the position of the dipole enables the sum of the dipole emission and reabsorption to be obtained, yielding the position dependence of photon recycling in the solar cell.

The complexity of the structure makes photon recycling computationally demanding, and this calculation is usually performed for a single-nanowire solar cell device. The calculation for one free-standing nanowire with a diameter of 400 nm and length of 2  $\mu\text{m}$  takes about 500 CPU hours (64-bit, 12 core AMD Opteron 6172) [70].

No publications have been found on photon recycling for nanowire arrays. A more practical version of this method is to ignore photon recycling and assume that all the internally emitted light exits the nanowire array without reabsorption. The light emission can then be calculated together with the electrical loss using

experimentally determined semiconductor parameters. This will be discussed in detail in Chapter 4 with respect to electrical modelling.

### 3.3. Optical modelling of tandem solar cells

The S–Q analysis can be extended to tandem solar cells provided appropriate consideration is taken of photon recycling between different cells. When calculating the single junction S–Q limit, a perfect mirror is assumed under the solar cell such that light emission is considered only on the top. In the case of a tandem cell with a double junction, emission from one subcell to the neighbouring semiconductor or to the air must be considered. Figure 14a shows a schematic illustration of a thick double-junction solar cell on a substrate. A high-bandgap p-n junction is placed on top of a low-bandgap one to create a tandem cell. Both junctions are III-V semiconductors with a refractive index of approximately 3.5 at a wavelength close to the bandgap wavelength. The primary emission is at wavelengths around the bandgap due to the carrier density distribution [93]. The emission from the top cell to the bottom cell is absorbed in the bottom cell or passes into the substrate. The primary emission from the bottom cell is below the bandgap of the top cell without inter-band absorption. The emission from the bottom cell exits into the air, with a high degree of reflection. The reflected fraction of the emission recycles to the bottom cell without optical loss, if it is assumed, as before in this section, that there are no non-radiative recombination processes in the bottom cell. The optical loss equals the emission to the top cell minus the reflection at the interface. This schematic analysis can be applied to thick cells but not to cells with a thickness close to the wavelength of incident light.

To calculate this emission loss, the principle of optical reciprocity for a solar cell with perfect absorptance was applied, and all photon recycling between the top and bottom cells was ignored [Papers I, III].

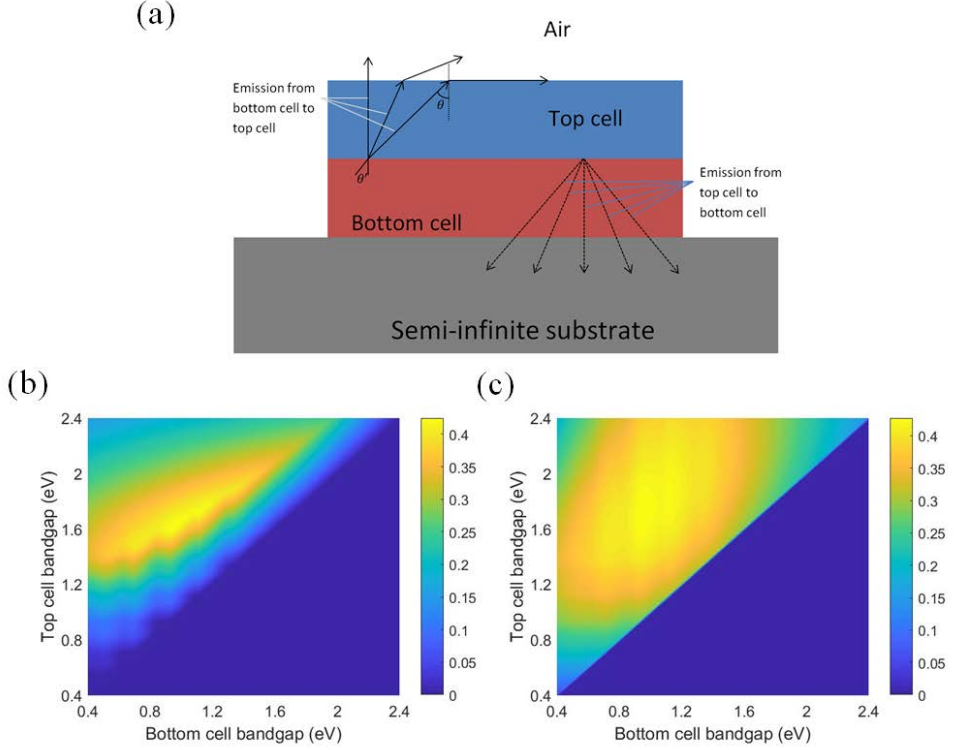


**Figure 14.** (a) Schematic illustration of interface radiation in a double-junction tandem solar cell ( $\theta$  is the angle of total internal reflection). (b) Series-connected double-junction solar cell. (c) Separately connected double-junction solar cell.

Under these assumptions, and assuming perfect absorption in the top and bottom cells, the double-junction S-Q equations are:

$$F_{c0,up(down),1(2)} = 2\pi c \int_0^{\lambda_{1(2)}} d\lambda \left[ \frac{n_{up(down),1(2)}^2}{\lambda^4 (\exp(2\pi\hbar c / \lambda k_b T) - 1)} A_{up(down),1(2)}(\lambda) \right] \quad (21a)$$

$$j_{1(2)} = \frac{e}{2\pi\hbar c} \int_0^{\lambda_{1(2)}} d\lambda [\lambda I_{AM1.5}(\lambda) A_{1(2)}(\lambda)] - e(F_{c0,up,1(2)} + F_{c0,down,1(2)}) [\exp\left(\frac{eV_{1(2)}}{k_b T}\right) - 1] \quad (21b)$$

$$\eta_{series} = \frac{\min\{j_1, j_2\}(V_{1max} + V_{2max})}{\int_0^\infty I_{AM1.5}(\lambda) d\lambda} \quad (21c)$$

$$\eta_{separately} = \frac{(j_1 V_{1max} + j_2 V_{2max})}{\int_0^\infty I_{AM1.5}(\lambda) d\lambda} \quad (21d)$$

where the subscripts *1* and *2* denote the top and bottom cell, and *up* and *down* specify the emission direction of each cell, for instance,  $F_{c0,up,1}$  describes the emission constant for the top cell towards the top of the cell.  $A_{up(down),1(2)}(\lambda) = 1$  under the assumption of perfect absorption, and  $\eta_{series}$  and  $\eta_{separately}$  are the efficiency of series and separately connected cells. Further equations for tandem cells with more junctions can be found in Ref. [10].

Figures 14b and c show two efficiency limit plots. The efficiency limit decreases rapidly for series connected\* cells with increasing top bandgap as a result of the contribution of current matching in the series-connected case, while for separately connected\* cells, the value decreases slowly. The peak efficiency of separately connected cells is about 1% higher than for series-connected cells under a one sun AM1.5G solar spectrum, due to this difference in current matching [15]. The figures show only the region where the top cell bandgap is greater than the bottom one. As it was assumed that the absorptance of photons above the bandgap was 1, the lower bandgap in the top cell than in the bottom cell leads to a lack of absorption in the bottom cell. This yields zero efficiency in the series-connected case and single-junction efficiency in the separately connected case. Neither provides any additional information about tandem cells vs. single-junction cells.

In a real tandem solar cell device, the imperfect absorption spectrum must be taken into consideration, i.e.,  $A_{up(down),1(2)}(\lambda) \neq 1$ . Let us consider a nanowire array with two p-n junctions, as shown in Figure 15a. Another tunnelling junction,

known as the Esaki diode [94], is used between the two p-n junctions to connect the cells. The thickness of this diode is usually about 50 nm. In optical modelling, the absorption in this diode is ignored. The absorption in the nanowire structure can be calculated for both the top and bottom cells with the scattering matrix method.

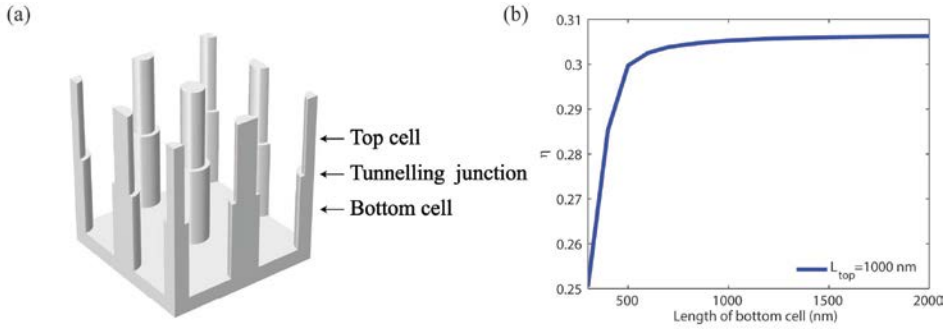


**Figure 15.** (a) Schematic illustration of a series-connected nanowire double-junction tandem cell. (b) Efficiency of a nanowire array double-junction cell as a function of bottom cell length, with a pitch of 200 nm. The nanowire diameter of top cell is 100 nm and nanowire diameter of bottom cell diameter is 200 nm.

In this structure, there are 5 parameters that can be changed independently: the diameters and lengths of the top and bottom cells, as well as the pitch. A parameter sweep for all combinations of these 5 parameters would be extremely computationally demanding, and is beyond current resources. Optimization methods are therefore used to reduce the calculation workload.

One direct approach is to use the steepest-descent method to calculate the efficiency through Equation (21), and then its gradient. In this case, the calculation would proceed in the direction of increasing gradient to the highest value. The conjugate gradient method is a modified version of the steepest-descent method, in which a more computationally convenient way of selecting the direction is used. The quasi-Newton method, the Levenberg–Marquardt algorithm, and many other

methods are based on first- or second-order derivatives. However, derivative-based methods fail in optimizing the efficiency of nanowire dual junction solar cells, as described below.

Figure 15b shows the results of a single parameter sweep over the length of the nanowire array for the bottom cell. The efficiency approaches a constant value as the bottom cell length is increased. This behaviour originates from the current matching of series-connected solar cells, i.e., when the other parameters are fixed and only the bottom cell length is increased, increasingly more photons are absorbed in the bottom cell, while the optical carrier generation in the top cell remains virtually unchanged. Due to the current matching in Equation (21) for series-connected cells, the current through the device is limited by the optical generation in the top cell such that the solar cell efficiency reaches a limit. From the numerical side, this slowly changing region in Figure 15b leads to a numerical derivative close to zero. As a result, optimization methods that depend on derivatives fail.

A direct iteration optimization method was used instead [Paper I]. The flow chart of the iteration is shown in Algorithm 1 below. In this method, each parameter is swept independently until no higher value can be obtained in any parameter dimension; the parameter combination then corresponds to a local maximum. With the knowledge of the efficiency maxima originating from the eigenmode resonances, both the  $HE_{11}$  and  $HE_{12}$  maxima can be achieved with different initial parameters in the iteration. The initial values of parameters can be estimated from Equation (7) using parameters from optical studies on the single-junction cell [89].

### **Algorithm 1**

Choose  $L_{top}$  to solve for.

Define variable names as follows:  $x_1 = D_{top}$ ,  $x_2 = D_{bot}$ ,  $x_3 = P$ ,  $x_4 = L_{bot}$

Define current point ( $x_{1,c}$ ,  $x_{2,c}$ ,  $x_{3,c}$ ,  $x_{4,c}$ ) *%starting point for iteration*

$\eta_{prev} = 0$  *%efficiency value in previous iteration step*

optimum\_not\_found=1

While(optimum\_not\_found)

$x_{4,prev} = x_{4,c}$  *%to find derivative  $d\eta/dx_4 = d\eta/dL_{bot}$  for which we set a limit of  $0.001 \mu m^{-1}$*

For  $i=1$  to 4

Define parameter limits,  $x_{i,lb} \leq x_i \leq x_{i,ub}$ , and step length  $x_{i,step}$

*%typically  $D_{top} < P$ ,  $D_{top,step} = 5 \text{ nm}$*

*%typically  $D_{bot} < P$ ,  $D_{bot,step} = 5 \text{ nm}$*

*%typically  $P < 2000 \text{ nm}$ ,  $P_{step} = 10 \text{ nm}$*

*%typically  $L_{bot} < 10000 \text{ nm}$ ,  $L_{bot,step} = 100 \text{ nm}$*

$\eta_{max} = 0$  *% maximum value of efficiency found in iteration over  $x_i$*

For  $x_{it}=x_{i,lb}$  to  $x_{i,ub}$  in step of  $x_{i,step}$

Compute  $A_1(\lambda)$  and  $A_2(\lambda)$  for  $\lambda < \lambda_2$  with  $x_i = x_{it}$  (using  $x_j = x_{j,c}$  for  $j \neq i$ )

Compute efficiency  $\eta$  for  $A_1(\lambda)$  and  $A_2(\lambda)$  *%Equations (S1)-(S6)*

If  $\eta > \eta_{max}$

$\eta_{max} = \eta$

$x_{i,c} = x_{it}$  *%updates current optimized geometry point --- affects iteration when moving from  $i$  to*

*$i+1$  in for loop)*

end

end

$\eta_i = \eta_{max}$  *% stores efficiency from iteration over  $x_i$*

end

if  $(\eta_1 - \eta_{prev}) < 0.0001$  &&  $(\eta_2 - \eta_{prev}) < 0.0001$  &&  $(\eta_3 - \eta_{prev}) < 0.0001$  &&  $(\eta_4 - \eta_{prev}) / (x_{4,c} - x_{4,prev}) <$

$0.001 * 1e6$

optimum\_not\_found=0 *%ends iteration since increase in eta smaller than set limit*

end

$\eta_{prev} = \eta_4$

end

*% $\eta_{prev}$  contains now the maximum efficiency after iteration and ( $x_{1,c}$ ,  $x_{2,c}$ ,  $x_{3,c}$ ,  $x_{4,c}$ ) optimized geometry*

*Pseudocode from Paper I.*



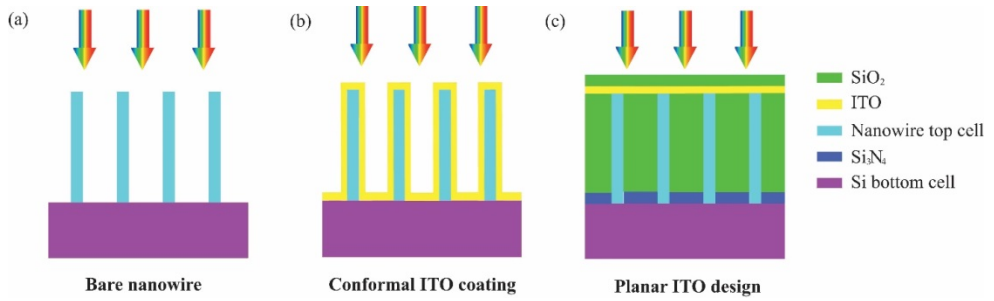


**Figure 16.** (a) Bare nanowire on silicon double-junction. (b) Conformal coating of indium tin oxide (ITO) contact on nanowires. (c) Planar ITO design with ARC. (Figure reprinted from Paper III with permission from OSA Publishing.)

Besides nanowire-on-nanowire double-junction solar cells, the nanowire-on-silicon double-junction solar cell is also a candidate for nanowire solar cell applications as shown in Figure 16. Due to lattice mismatch tolerance and highly developed silicon technology, the nanowire-on-silicon double-junction cell is designed to yield high efficiency at a lower cost than double-junction nanowire cells.

Early modelling was primarily carried out for nanowire arrays on top of an infinite silicon substrate to study the optical response and optimize the absorption in both junctions. The efficiency of this structure was limited by two potential problems: one is the contact design for the nanowire-on-silicon cells, and the other is that the planar silicon–nanowire array interface introduces additional light reflection between the bandgap of silicon and the high-bandgap nanowire array material.

Considering the electrical contact of ITO, we proceed from the nanowire-on-silicon design to conformal coating. With the dimensions optimized for absorption in the nanowire array, the nanowire was coated with ITO, as shown in Figure 16b. The thickness of the ITO coating was taken from previous experimental work [59]. In the case of nanowires on silicon, the nanowires are quite close to each other, compared to previous studies on single-junction nanowire array cells. Conformal

coating led to a large volume of ITO in the contact layer, and such an ITO coating absorbs about 50% of the photons between the bandgap of silicon and the nanowire material [Paper III].

To reduce the amount of ITO used, a planar ITO structure was adopted, as shown in Figure 16c. This kind of planar top surface increases the reflection. The total reflection between the nanowire material and silicon bandgap was 20-30%, and above the nanowire material bandgap it was 10%. Two layers of ARC were applied, one of  $\text{SiO}_2$  on the top of what to reduce the reflection above the nanowire material bandgap, and the other of  $\text{Si}_3\text{N}_4$  at the nanowire-silicon interface, to reduce the reflection between the bandgaps of nanowire material and silicon. After applying these two ARCs, the reflection losses were reduced by 80%. Further technical details can be found in Paper III.



## 4. Electrical modelling

The main topic of the previous chapter was light absorption in a nanowire array. Optical recombination based on purely optical considerations can be applied to a solar cell. An ideal solar cell model based on S-Q analysis was studied with radiative recombination only. In reality, after electron-hole pairs are photogenerated in the semiconductor, various recombination channels contribute to carrier loss, reducing the performance of the device. Semiconductor physics modelling was used to simulate these processes.

### 4.1. Electrical modelling at zero bias

This chapter starts with a brief introduction to the drift-diffusion semiconductor model. This model can be derived from, and is an approximate solution to, the Boltzmann transport equation. The derivation of the equations is not discussed in detail here, but the assumptions and physical meaning of the assumptions used in this work are listed below[95].

- a) Non-degenerate approximation: Fermi energy is assumed to be more than  $k_bT$  below/above the conduction/valence band edge; otherwise the state filling, due to the intrinsic properties of fermions, leads to the failure of Boltzmann statistics. In addition, this method can be extended to slightly degenerated semiconductors. The validity has been double-checked with the solution to the Boltzmann transportation equation. Studies have shown that for a degenerated semiconductor, the solution to the slightly extended

drift-diffusion equations agrees with solutions from the Boltzmann transportation equation [96].

- b) Parabolic band assumption: The energy bands are parabolic close to the band edge where  $E = \hbar^2 k^2 / 2m^*$ .
- c) Steady-state or quasi-equilibrium state assumption (for steady-state solution): The drift-diffusion model yields the solution for the time-independent system. Moreover, the thermal relaxation process is treated as an ‘infinitely rapid’ process, i.e., it is assumed, for example, that all photo-generated electrons and holes are generated into the thermal distribution of the semiconductor.

Based on these approximations, the drift-diffusion model can be written as a set of equations including Poisson’s equation (a) and drift-diffusion equations for electrons (b) and holes (c):

$$\nabla \cdot (-\varepsilon_{stat} \nabla \varphi) = e(p - n + N_d - N_a) \quad (22a)$$

$$\nabla \cdot J_n = \nabla \cdot (-e\mu_n n \nabla \varphi_n) = e(R - G) \quad (22b)$$

$$\nabla \cdot J_p = \nabla \cdot (-e\mu_p p \nabla \varphi_p) = -e(R - G) \quad (22c)$$

where  $\varepsilon_{stat}$  is the static dielectric function,  $q$  is the elementary charge,  $\mu$  is the carrier mobility,  $n/p$  denotes the electron/hole concentration,  $\varphi$  is the static potential,  $\varphi_{n/p}$  denotes the electron/hole potential and  $N_{d/a}$  denotes the concentration of ionized donors/acceptors. At room temperature with a thermal energy of about 25 meV, the ionization of dopants is usually assumed to be complete, and the concentrations of ionized donors and acceptors equal the doping levels.  $G$  is the optical generation rate calculated from Equation (14), and  $R$  is the net recombination rate.

In these equations, the unknown variables are the potential functions  $\varphi$  and  $\varphi_{n/p}$ . From semiconductor constants that can be found in handbooks or references, or

assumed for the particular system of interest, the total electron/hole concentration  $n/p$  and recombination rate  $R$  can be calculated based on  $\varphi$  and  $\varphi_{n/p}$ .

To calculate the carrier density, the band diagram that generates the density of states and the distribution functions must be determined. For electrons and holes, which are fermions without strong correlation, the distribution function obeys the Fermi–Dirac distribution:

$$f(E, E_{F_{n/p}}) = \frac{1}{\exp\left(\frac{\pm(E - E_{F_{n/p}})}{k_B T}\right) + 1} \quad (23)$$

where  $E_{F_{n/p}}$  is the quasi-Fermi level of the electron/hole and the ‘ $\pm$ ’ signs refer to electrons/holes respectively. Note that this use of the Fermi–Dirac distribution extends the drift diffusion equations to (slightly) degenerate semiconductors and reduces to the Boltzmann distribution in the limit of a non-degenerate semiconductor. In a nanowire solar cell, the typical diameter is around 200 nm, which is still not of the order of a one-dimensional wire considering the density of states. A three-dimensional density of states can however, still be used as an approximation:

$$D_n(E) = \frac{1}{2\pi^2} \left(\frac{2m_n^*}{\hbar^2}\right)^{3/2} \sqrt{E - E_c} \quad (24a)$$

$$D_p(E) = \frac{1}{2\pi^2} \left(\frac{2m_p^*}{\hbar^2}\right)^{3/2} \sqrt{E_v - E} \quad (24b)$$

where  $m_{n/p}^*$  denotes the effective mass of an electron/hole in the conduction/valence band and  $E_{c/v}$  is the band edge of the conduction/valence band. Thus, the electron and hole densities can be written concisely as:

$$n = \int_{E_c}^{\infty} f(E, E_{F_n}) D_n(E) dE = N_c F_{\frac{1}{2}}\left(\frac{E_{F_n} - E_c}{k_B T}\right) \quad (25a)$$

$$p = \int_{-\infty}^{E_v} f(E, E_{F_p}) D_p(E) dE = N_v F_{\frac{1}{2}}\left(-\frac{E_{F_p} - E_v}{k_B T}\right) \quad (25b)$$

$$N_{c/v} = 2 \left( \frac{m_e^* / h}{2\pi h^2} k_B T \right)^{3/2} \quad (25c)$$

where  $F_{1/2}$  is the Fermi integral as defined by:

$$F_{\frac{1}{2}}(\eta) = \frac{2}{\sqrt{\pi}} \int_0^\infty \frac{x^{1/2}}{1 + \exp(x - \eta)} dx. \quad (26)$$

Once the carrier density has been defined, the only remaining parameter is the recombination rate,  $R$ . Recombination in a semiconductor is usually classified according to the associated physical process, as illustrated in Figure 17.

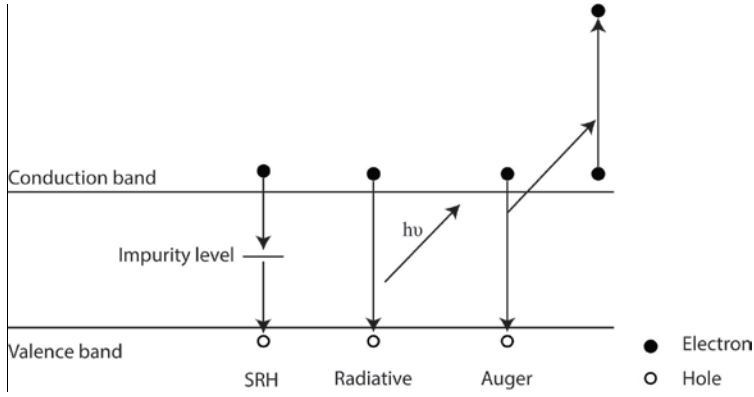


**Figure 17.** The recombination processes that can take place in a semiconductor: SRH, radiative recombination and Auger recombination.

In 1952, a kind of impurity-based recombination in semiconductors was studied by W. Shockley and W. T. Read [9]. In the same year, R. N. Hall verified this experimentally by studying the carrier recombination in Ge [97]. The SRH recombination process is named after these three scientists. The electron is excited to an impurity state where it recombines with the hole in the valence band, releasing phonons. The original expression for the SRH recombination rate is [9]:

$$R_{\text{SRH}} = \frac{pn - p_1 n_1}{\tau_p(p + p_1) + \tau_n(n + n_1)} \quad (27)$$

where  $\tau_n$  and  $\tau_p$  are the times during which an electron or a hole is captured by all the empty/filled trapping states,  $N_t$ , is the density of trapping states, and  $p_1/n_1$

is the carrier concentration at which the Fermi level is located at the energy of the trapping state. It is usually difficult to calculate  $\tau_{n/p}$  from theory, although many experiments have been performed to extract the average value. In reality, the scattering time depends on the impurity density, both of which are difficult to estimate. The scattering time has been reported to be of the order of microseconds to nanoseconds in previous studies [70, 98, 99]. If we assume that:

- a) all the trapping states have the same energy, which is equal to the intrinsic Fermi level of the semiconductor, and that
- b) electrons and holes have the same scattering time, or  $\tau_n = \tau_p$ ,

Equation (27) can be simplified to:

$$R_{\text{SRH}} = \frac{A(np - n_i^2)}{n + p + 2n_i}. \quad (28)$$

For band-to-band radiative recombination, the total radiative recombination rate is proportional to the densities of both kinds of carriers, giving  $R_{\text{total}} = Bnp$ . In the equilibrium state, radiative recombination is balanced by the thermal generation of electron-hole pairs. In this case, the total recombination rate is  $R_{\text{total}}' = G_{\text{thermal}} = Bn_i^2$ , where  $n_i$  is the intrinsic carrier density. In the non-equilibrium state, the thermal generation rate is the same as that at room temperature. The net radiative recombination is thus the difference between the total recombination rate and thermal generation rate:

$$R_{\text{rad}} = B(np - n_i^2). \quad (29)$$

Note that in the above, it was assumed that the value of  $B$  does not vary with  $n$  and  $p$ .

In a semiconductor, it is possible for an electron to recombine with a hole and transfer its energy to another electron in the conduction band. This is known as Auger recombination, and the recombination rate can be written:



$$R_{\text{Aug}} = C(n + p)(np - n_i^2) \quad (30)$$

assuming that the electron and hole have the same Auger lifetime.

Including SRH, radiative and Auger recombination, introduces three semi-empirical parameters  $A$ ,  $B$  and  $C$ , into the model.

Apart from the recombination processes described above, surface recombination is also an important recombination channel, especially for nanostructures with a large surface-to-volume ratio. Surface recombination may be treated as a special case of SRH recombination involving surface states instead of impurity states inside the material. The surface recombination velocity,  $V_{\text{sr}}$ , is normally used to describe this, and the surface recombination rate is written as:

$$R_{\text{surface}} = \frac{V_{\text{sr}}(np - n_i^2)}{n + p + 2n_i} \quad (31)$$

using the same assumptions as in bulk SRH recombination above. No surface charge or state filling was considered in the modelling described in this thesis.

The contributions from all four types of process should be included in the total recombination rate at a given spatial position. In other words, at the nanowire surface, the contributions from Equations (28) to (31) should be considered, and inside the nanowire, Equations (28) to (30) should be considered. Using these recombination and carrier concentration calculations, it is possible to solve the drift-diffusion Equations (22) using, for example, the FEM method in the Comsol Partial Differential Equation (PDE) module. A valence band offset can also be applied in the band structure calculation to simulate a semiconductor heterojunction. Further details can be found in Paper II.

In order to simulate a solar cell, this drift-diffusion model must be combined with the optical model. The optical generation rate was calculated with the Wave Optics module in Comsol to obtain the position-dependent optical generation rate. This function was inserted into the drift-diffusion model to calculate the current.

To further explain the results, a position-dependent electron–hole splitting efficiency, denoted the spatial internal quantum efficiency (SIQE), was introduced [100] [Paper II]. In this analysis, a 10 nm cubic box was inserted into the nanowire and optical generation was induced in this box. The photogenerated electron–hole density was set to the level of optical generation in the InP nanowire array under one sun illumination, typically between  $10^{26}$  and  $10^{29} \text{ m}^{-3}\text{s}^{-1}$ , as shown in Figure 12. In this region, the splitting efficiency can be treated as a constant. The current resulting from this generation can be obtained by solving the drift diffusion equations (Eq. (22)) in this small box only. The ratio between the extracted carriers and total electron–hole pairs in the cubic box yields the SIQE of the nanowire solar cell at this position. This is a function of the box position and also depends on the structure of the p-n junction. This analysis provides information on the inside of a NWASC with spatial resolution, helping in the design of the solar cell. A similar experimental method, known as the electric-beam-induced current (EBIC) method, has been used to obtain further information on the nanowire p-i-n junction [101, 102]. An electric beam is used to excite electron–hole pairs at a fixed position, and the current is measured with different excitations at various positions across the p-i-n junction.

When sweeping the cubic box over the nanowire p-i-n junction, as in the EBIC method, a large carrier loss in the contact was found in the top n-doped segment of the InP NWASC. The electric field remained at a relatively high value across the intrinsic part which is depleted. In contrast, in the p- and n-doped segments, no such electrical field was found, and minority carriers will diffuse to the contact with increasing probability the closer they come to the contact, which leads to a decrease in the SIQE towards the contact [59, 67] [Paper II]. From the optical generation shown in Figure 12, it can be seen that most of the optically generated carriers are found in a short segment at the top of the nanowire. Thus, to obtain a higher current and internal quantum efficiency, the top n-doped segment should be shorter. In reality, to make a good contact to nanowires, a very thin top doped

segment in a planarized nanowire array design is difficult to contact. A segment length of about 60 nm is required in the nanowire array due to the standard deviation in nanowire length, while the thickness of the top dope segment in a single-junction thin-film GaAs cell is at present 30 nm.

To eliminate this limitation, a front side barrier can be introduced to prevent holes from reaching the top contact. A gradient doping profile in the n segment helps reduce contact recombination, but increases the Auger recombination due to the increased doping level. It is thus difficult to reduce the top contact loss with a gradient doping profile without introducing additional recombination.

Nanowires reveal their advantage of high lattice mismatch tolerance in direct growth, as mentioned previously. Let us consider a nanowire heterojunction with a bottom InP p-i and a top GaP n junction. The high-bandgap GaP segment suppresses optical generation in the top n-doped segment such that most optical generation occurs instead in the intrinsic part, with high internal quantum efficiency. The inset in Figure 18a shows 1D optical generation in this structure along the radial direction. As SIQE is close to 100% in the intrinsic region, the total internal quantum efficiency can be increased to almost 100%. Another benefit of this design is that it allows for a longer n-doped segment of 100 nm, without further loss due to contact leakage, thanks to the high bandgap of GaP [Paper II]. A longer top segment could be beneficial in device fabrication.

A top segment of high-bandgap GaP provides an efficient barrier for minority carriers on the top, but the bottom contact leakage still limits the open-circuit voltage [Paper V]. As shown in Figure 18b, introducing only a top GaP selective contact seldom improves open-circuit voltage due to the high leakage from the bottom contact. Using a GaP substrate instead of an InP substrate, increases the open-circuit voltage to 0.97 V, with a non-radiative lifetime of 100 ns. If we assume perfect lattice and surface quality, the open-circuit voltage increases to 1.02 V, which is the S-Q value.

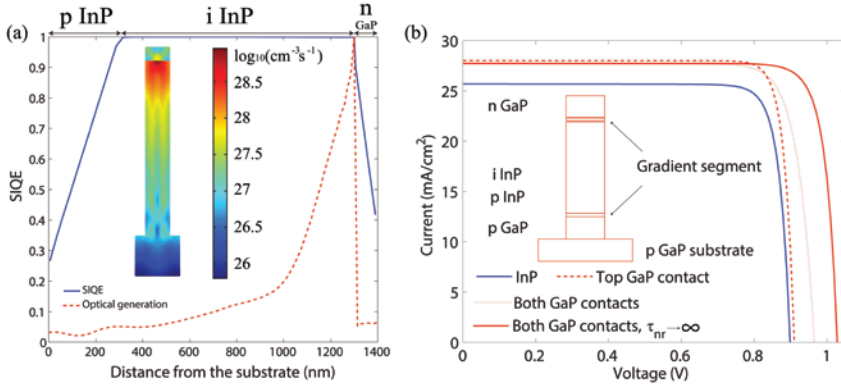


**Figure 18.** (a) Optical generation and SIQE of an InP-GaP p-i-n junction solar cell (figure from Paper II with permission from copyright owner). (b) I-V response of an InP-GaP p-i-n junction solar cell on a p-type GaP substrate (figure from Paper V with permission from copyright owner).

## 4.2. I-V modelling in the 1D and 3D models

Using the 3D electrical modelling described in the previous section, solar cells can be optimized through a large number of parameter sweeps. However, the calculation time is a limiting factor. The calculation time for one I-V curve in the 3D model is approximately one hour on a Dell laptop (Latitude 14 7000 Series Ultrabook™ [E7440]). A more powerful computational resource, such as a Dell workstation with 32 CPU cores, or a cluster, could be used, but the speed of FEM calculations does not scale well with increasing number of CPU cores. For example, when running the FEM calculations in Comsol, increasing the number of cores from 6 to 24 reduced the computational time by only 50-67%, not by 75%. It was also found that the reduction in computational time was less when several instances of Comsol were run in parallel on one physical computer or workstation.

The computational time could be reduced by using an effective 1D model for a NWASC. In order to do this, the optical generation rate in the 3D model was calculated and integrated over the cross-section of the nanowire, as shown in

Figure 18. This optical generation was then used as the input for the 1D drift-diffusion model, which averages the optical generation in the bulk for each axial position. The SRH, radiative and Auger recombination rates are the same as in the 3D model.

The 1D bulk model differs from the 3D nanowire model in its surface recombination. In the 3D model, surface recombination is included through a current flux term through the surface. The same flux intensity is set for electrons and holes to retain carrier balance in the nanowire. Figure 19a shows the importance of this surface recombination for solar cell current. At surface recombination velocities higher than  $10^5$  cm/s, the short-circuit current of the solar cell decreased rapidly. InP nanowires, which have been reported to have an ultralow surface recombination velocity of 170 cm/s, are a suitable for NWASCs [103]. A high-bandgap material must be used for surface passivation in a GaAs NWASC, as unpassivated GaAs has a high surface recombination velocity up to  $10^7$  cm/s.

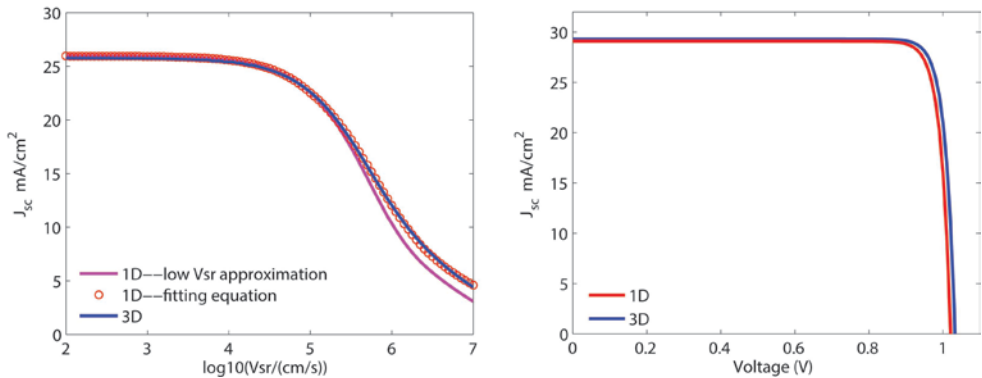


**Figure 19.** (a) Short-circuit current of an InP NWASC as a function of surface recombination velocity for the 3D and 1D models. Solid red line:  $A_0=2$ , dotted red line:  $A_0$ , from Equation (34). (b) 3D and 1D current–voltage response of an InP NWASC including radiative recombination only. Parameter  $B=1.2 \times 10^{-10}$  cm<sup>3</sup>/s (from [104]).

There is no nanowire side surface in the 1D model, and it is therefore impossible to consider the surface recombination in the same way as in the 3D model. A

semi-numerical fit of the analytical solution from surface recombination to bulk SRH-like recombination has been performed in previous studies [105, 106]. Following their work, the following equations were employed [106] [Paper V]:

$$A_{\text{surface}} = A_0 \frac{V_{\text{sr}}}{r} \quad (32)$$

$$A_0 = \min\left[\frac{1}{2} \log_{10}\left(\frac{V_0}{V_{\text{sr}}}\right), 2\right] \quad (33)$$

where  $r$  is the radius of the nanowire and  $V_{\text{sr}}$  is the surface recombination velocity. The parameter  $A_{\text{surface}}$  is used together with  $A_{\text{SRH}}$  in Equation (28) as  $A = A_{\text{surface}} + A_{\text{SRH}}$ . The parameter  $V_0$  can be found in Paper V.

Parameter fitting for the solution of analytical equations in a previous study yielded a value of 2 for  $A_0$  [106]. This is suitable in a regime of low surface recombination. Comparison of the results of 1D and 3D modelling in the present work showed that the proposed Equation (33) provided better numerical fitting for higher surface recombination.

Radiative recombination alone can be considered in the drift-diffusion model by “switching off” SRH, surface and Auger recombination, and contact leakage. The results of 3D and 1D modelling are shown in Figure 19b. In this case, open-circuit voltage is 1.02 V for the 3D model and 1.03 V for the 1D model. These values are quite close to the S–Q limit for bulk InP, which is 1.02 V under one sun AM1.5G spectrum. These results, both with and without non-radiative recombination, verify the validity of the 1D and 3D drift-diffusion models.

In the region where the voltage is less than 0.9 V, the 1D and 3D IV models agree very well, however, slight differences are seen at higher applied voltages. These originate from the shape of the substrate. In 1D modelling, only the nanowire cross-sectional area,  $\pi r^2$ , is considered for the substrate, while in 3D modelling, a substrate region that has an area equal to the unit cell area of the

square array is modelled. As the bottom contact has the same area as the substrate, this leads to differences in the carrier injection at higher voltages.

To illustrate the difference in carrier injection, the dark current was calculated with both the 1D and 3D models, and is shown in Figure 20. In Figure 20a, where the contact is at the bottom of the substrate, the difference in injection occurs at a voltage of about 0.9 V, and increases with increasing voltage. The current predicted by the 1D model is lower than that predicted by the 3D model, as the contact area is smaller in the 1D than in the 3D model, leading to lower current injection. In Figure 20b, where the contact is at the bottom of the nanowire instead, the 1D and 3D models give almost the same results over the whole voltage range. Note that Figure 20 shows the dark current as no photogeneration occurs. In the case of illumination, the current originates predominantly from photogenerated carriers rather than contact injection when the applied voltage is lower than the open-circuit voltage. Hence, the 1D model is in quite good agreement with the 3D model, which includes the substrate, as shown in Figure 19b.

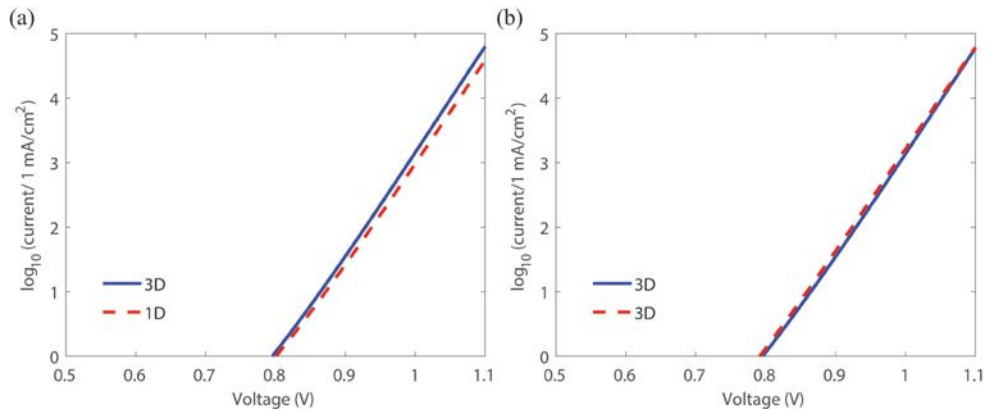


**Figure 20.** Dark current predicted by 3D and 1D modelling. (a) Contact at the bottom of the substrate. (b) Contact at the bottom of the nanowire. The surface recombination velocity was set to 0 in the calculations.

Analysis of the I-V response at zero surface recombination velocity using this accurate 1D model, allows the study of the realistic case of non-zero surface recombination velocity. At low surface recombination velocity, the carrier concentration can be considered to be constant along the radial direction, resulting in the following expression.

$$\pi r^2 R_{\text{bulk}} = 2\pi r R_{\text{surface}} \quad (33)$$

Substituting Equations (28) and (31) into Equation (33) yields the effective surface recombination (Equation (32)) with a constant,  $A_0$ , of 2, which agrees with the previously published value [106].

At high surface recombination velocity, assuming the carrier concentration to be constant along the radial direction is not a good approximation due to surface band bending. This band bending leads to less recombination at the surface, as can be seen in Figure 19a.





## 5. Light emission and photon recycling

The previous two chapters described how optical absorption and electrical carrier extraction were used to calculate the solar cell I-V response and efficiency. Non-radiative recombination is considered to be the major source of loss in these cells. Radiative recombination is taken into account either through optical reciprocity or the semiconductor recombination parameter. Both of these methods have limitations when assessing photon recycling in a solar cell.

In the optical analysis using Lorentz reciprocity, the light emission is calculated from the reciprocity between two dipoles [107]. Typical calculations give the far-field emission of the solar cell. The calculation of photon recycling is not easily performed in such an analysis, as the computation of the optical near-field is required to calculate the absorption/recycling of the photons emitted within the solar cell.

The light emission can also be calculated with directional Kirchhoff reciprocity [93]. The absorptance is equal to the emissivity along a fixed direction of the studied structure. As this directional law requires the description of geometric optics and the exclusion of evanescent waves, it can only be used to obtain the far-field emission [91], and provides no information on photon recycling.

The emission of light can also be calculated by the solution to semiconductor equations. Firstly, the carrier concentrations are calculated by solving the drift-

diffusion equations. Then, the light emission is included through the parameter for radiative recombination, which can be found in semiconductor handbooks for bulk materials. It is then possible to calculate the near-field emission and photon recycling [70]. However, the calculation from semiconductor equations also suffers from clear disadvantages. Tabulated radiative recombination parameters have been measured in bulk semiconductors. In nanostructures, the radiative recombination parameter changes not only with different materials, as in bulk-like systems, but also with the shape of the structure. This is known as the Purcell effect. That is to say, the radiative recombination parameter,  $B$ , is not constant, but is a function of position and wavelength  $B(\mathbf{r}, \lambda)$ . Therefore, calculations based on the bulk semiconductor recombination parameter are not accurate for nanostructures since the Purcell effect is neglected.

This chapter describes a self-consistent model based on drift diffusion and the dyadic Green's functions. The light emission from a periodic NWASC can be calculated, allowing photon recycling in the solar cell to be studied.

## 5.1. Dyadic Green's functions and power flow

The definitions of dyadic Green's functions are [108]:

$$\nabla \times \nabla \times \vec{G}^E(\vec{r}, \vec{r}', \omega) - k_0^2 \epsilon_s(\omega) \vec{G}^E(\vec{r}, \vec{r}', \omega) = \vec{I} \delta(\vec{r} - \vec{r}') \quad (34)$$

$$\nabla \times \nabla \times \vec{G}^H(\vec{r}, \vec{r}', \omega) - k_0^2 \epsilon_s(\omega) \vec{G}^H(\vec{r}, \vec{r}', \omega) = \nabla \times [\vec{I} \delta(\vec{r} - \vec{r}')] \quad (35)$$

where  $\vec{G}^{E/H}$  are the electric/magnetic Green's dyads,  $k_0$  is the wave vector in vacuum and  $\vec{I}$  is a unit tensor.

Using Equations (34) and (35), the solution for the electric and magnetic fields can be written:

$$\vec{E}(\vec{r}, \omega) = i\omega\mu_0 \int_V d\vec{r}' \vec{G}^E(\vec{r}, \vec{r}', \omega) \cdot \vec{J}(\vec{r}', \omega) \quad (36)$$

$$\vec{H}(\vec{r}, \omega) = \int_V d\vec{r}' \vec{G}^H(\vec{r}, \vec{r}', \omega) \cdot \vec{J}(\vec{r}', \omega) \quad (37)$$

where  $\vec{J}$  is the radiation source of current.

Thus, the ensemble-averaged Poynting vector can be expressed as (where *c.c.* denotes the complex conjugate):

$$\begin{aligned} \langle \vec{S}(\vec{r}, \omega) \rangle &= \frac{1}{2} \text{Re}(\langle \vec{E} \times \vec{H}^* \rangle) \\ &= \frac{i\omega\mu_0}{4} \iint_V d\vec{r}_1^3 d\vec{r}_2^3 \varepsilon_{ijk} \left\langle \vec{G}_{jm}^E(\vec{r}, \vec{r}_1, \omega) J_m(\vec{r}_1, \omega) J_l^*(\vec{r}_2, \omega) \vec{G}_{lk}^{H*}(\vec{r}, \vec{r}_2, \omega) \right\rangle + c.c. \end{aligned} \quad (38)$$

Two averages are applied in Equation (38). The power flow is averaged over time by applying the time-averaged Poynting vector. In addition to this average state, the system can occupy a number of possible states resulting from thermal fluctuations. The average over all these states is considered to be the ensemble average given in ' $\langle \rangle$ '.

We now assume that the dielectric function of the system is constant when considering thermal fluctuations. Green's dyads are then constant in the average over the different possible states, according to their definitions (Equations (34) and (35)). Consequently, the ensemble average in Equation (38) is transformed into the correlation function of dipole density.

$$\langle \vec{S}(\vec{r}, \omega) \rangle = \frac{i\omega\mu_0}{4} \iint_V d\vec{r}_1^3 d\vec{r}_2^3 \varepsilon_{ijk} \vec{G}_{jm}^E(\vec{r}, \vec{r}_1, \omega) \langle J_m(\vec{r}_1, \omega) J_l^*(\vec{r}_2, \omega') \rangle \vec{G}_{kl}^{H*}(\vec{r}, \vec{r}_2, \omega') + c.c. . \quad (39)$$

According to the fluctuation dissipation theorem, this dipole density correlation function can be calculated from Ref. [109] with refractive index and quasi Fermi level splitting.

This quasi-Fermi level splitting can be computed using the electrical modelling described in Chapter 4. The recycled photons introduce additional optically generated carriers and affect the quasi-Fermi level splitting. An iterative solution between the light-emission model and the drift-diffusion model is needed to achieve a convergent result.

Equations (34), (35), (39) and (40), together with electrical modelling using the drift-diffusion equations, form a complete set of equations with which it is possible to calculate the spontaneous emission from a nanostructured semiconductor solar cell. These equations can also be used to study the photon recycling in nanostructured semiconductor solar cells.

## 5.2. Numerical solution of Green's dyads in a periodic nanostructure

In the photon recycling calculation for nanostructured solar cells, one of the main computational problems lies in solving for the electric and magnetic Green's dyads in the periodic nanostructures.

Using Equations (36) and (37), the calculation of Green's dyads can be transformed into the numerical solution of the electric and magnetic fields by assuming

the current source to be a point dipole source. Green's dyads can thus be calculated using the FEM in the Comsol Wave Optics module. A set of Green's dyads can be calculated by varying the position of the dipole source in the semiconductor.

The periodic boundary condition is usually applied in a periodic nanostructure, to reduce the computational workload. However, this cannot be done in the calculation of Green's dyads in a periodic nanostructure, since this gives the same dipole source in every unit cell. The emission in a periodic nanowire array is instead calculated by considering an array of a finite number of nanowires and modelling the emission from the centre nanowire. The emission from a corresponding dipole in any other nanowire can be obtained by shifting such an emission pattern by an integer number of unit cells, as shown in Figure 21a. Similarly, the photon recycling in the nanowire can be calculated by shifting the power flow from neighbouring unit cells into the studied unit cell. (Tabulated values of the refractive index [110] were used in the calculations; the modification arising from the dipole source was not included.)

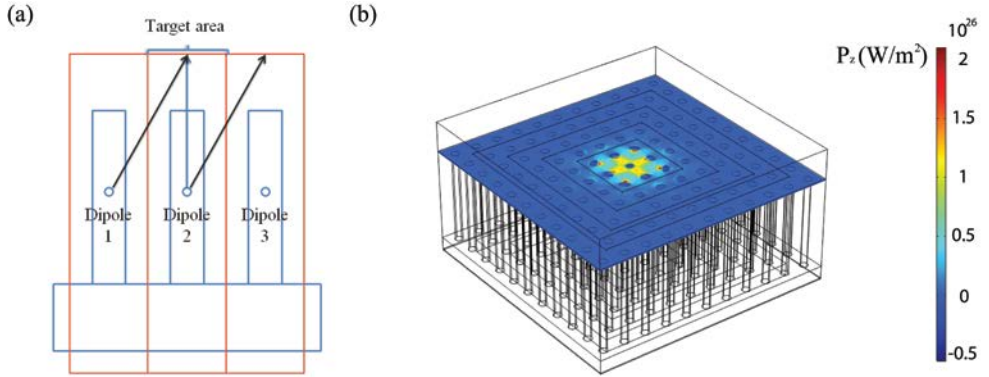


**Figure 21.** (a) Schematic illustration of a periodic nanowire array. The emission from Dipoles 2 and 3 is the same as from Dipole 1, but translated by one or two unit cells. (The red boxes indicate one unit cell.) (b) Dipole emission in an 11 x 11 InP nanowire array. The emission power is calculated assuming an  $x$ -polarized dipole in the middle of the centre nanowire.

Figure 21b shows an example of the dipole emission calculation in an  $11 \times 11$  InP nanowire array. Here, the power emission in the axial direction of the nanowire array from a dipole at the centre nanowire is considered. The power flow through this horizontal plane is plotted. The emission power is mainly found in a central region consisting of  $7 \times 7$  nanowires. The remaining region accounts for only a small contribution of 2.3%, although it occupies a larger space than the central  $7 \times 7$  nanowire region. In such an  $11 \times 11$  array, the discrepancy in the power flow calculation appears to be less than 1%, compared to the true value.

The power flow can be calculated with these Green's dyads and Equation (39). Photon recycling can also be calculated in the nanowire, by summing the power flow into and out of a small volume in the nanowire. The photon recycling data are added to the solar generation in the drift-diffusion Equations (22). Finally, solving the drift-diffusion equations gives the current-voltage response of the NWASC with photon recycling.

## 6. Conclusions and Outlook

Optical and electrical modelling has been used to study III-V NWASCs. Combined opto-electrical modelling was performed with the FEM method, while the pure optical modelling was performed with the scattering matrix method.

S-Q analysis was applied to dual-junction NWASCs. A lower limit for the solar cell efficiency was calculated under the assumption that emissivity is maximized. The geometric dimensions giving the highest efficiency were determined by employing an optimization method that did not depend on derivatives. Optical modelling of a nanowire-on-silicon double junction tandem structure was also performed. A planarized top contact layer was found to be beneficial in reducing the volume of ITO required in the device. This also reduced the absorption loss compared with a conformal contact design. In addition, two ARC layers were introduced to reduce the reflection beyond/below the bandgap energy of nanowire material, one on top of the ITO and the other at the silicon–nanowire interface. This reduced the reflection loss by 80%.

A single-junction InP NWASC was also studied by combined optical and electrical 3D modelling in the short-circuit case. SIQE was introduced as a tool to understand the internal electron–hole splitting process. Contact leakage was found to be an important current loss mechanism due to the absence of electric fields in the doped segments of the nanowire. Contact leakage could be suppressed by introducing a gradient in the doping profile of the n-doped top segment. However, the Auger recombination increased, which limited the total quantum yield. The high-bandgap semiconductor GaP was proposed as the top n-doped material,



pushing optical generation towards the high-SIQE intrinsic region and increasing the total electron–hole splitting efficiency to almost 100%. Furthermore, a significant improvement was achieved in the open-circuit voltage, close to Shockley–Queisser limit of 1.02 V, by adding a selective contact of GaP in InP NWASCs.

A computationally fast 1D model was developed to simulate the current–voltage response of NWASCs in order to reduce the computational demands. The results of this 1D modelling led to suggestions for experiments in both single-junction and tandem nanowire cells.

Light emission plays a significant role in solar cells. By combining Green’s dyads with the drift-diffusion equations, it was possible to develop a self-consistent model for calculations of spontaneous light emission and photon recycling in NWASCs. The emission power was calculated by summing the Poynting vector of the emission field at different positions. The Purcell effect in nanostructure was considered intrinsically in the calculations within the Green’s dyads.

However, from the optics modelling perspective, the application of nanowire arrays in tandem solar cells with more than 3 junctions has limitations. The limitation of low-bandgap subcells leads to the requirement of nanowires with a larger diameter, while the top cell requires a smaller diameter with a small pitch. It is experimentally difficult to fabricate a nanowire array with different diameters for different subcells in a monolithic device. One possible solution may be to use clusters of small-diameter nanowires in a subcell on top of a large-diameter nanowire subcell to create a tandem cell. This introduces additional dimensions to the nanowire array, and will require a better understanding of nanophotonics.

# References

1. BP: *Statistical Review of World Energy 2016*.
2. Gueymard, C.A., *Parameterized transmittance model for direct beam and circumsolar spectral irradiance*. Solar Energy, 2001. **71**(5): p. 325-346.
3. Gueymard, C.A., D. Myers, and K. Emery, *Proposed reference irradiance spectra for solar energy systems testing*. Solar Energy, 2002. **73**(6): p. 443-467.
4. Gueymard, C.A., *The sun's total and spectral irradiance for solar energy applications and solar radiation models*. Solar Energy, 2004. **76**(4): p. 423-453.
5. Kim, H.S., et al., *Lead iodide perovskite sensitized all-solid-state submicron thin film mesoscopic solar cell with efficiency exceeding 9%*. Sci Rep, 2012. **2**: p. 591.
6. Shuttle, C.G., et al., *Charge extraction analysis of charge carrier densities in a polythiophene/fullerene solar cell: Analysis of the origin of the device dark current*. Applied Physics Letters, 2008. **93**(18).
7. Draper, H.N., *Effect of Light on the Electric Conductivity of Selenium*. Nature, 1873. **7**: p. 303.
8. Shockley, W. and H.J. Queisser, *Detailed balance limit of efficiency of p-n junction solar cells*. Journal of applied physics, 1961. **32**(3): p. 510-519.
9. Shockley, W. and W. Read Jr, *Statistics of the recombinations of holes and electrons*. Physical review, 1952. **87**(5): p. 835.
10. De Vos, A., *Detailed balance limit of the efficiency of tandem solar cells*. Journal of Physics D: Applied Physics, 1980. **13**(5): p. 839.
11. Sandhu, S., Z. Yu, and S. Fan, *Detailed balance analysis and enhancement of open-circuit voltage in single-nanowire solar cells*. Nano letters, 2014. **14**(2): p. 1011-1015.
12. Sandhu, S., Z. Yu, and S. Fan, *Detailed balance analysis of nanophotonic solar cells*. Optics express, 2013. **21**(1): p. 1209-1217.
13. Green, M.A. and S.P. Bremner, *Energy conversion approaches and materials for high-efficiency photovoltaics*. Nature Materials, 2017. **16**(1): p. 23-34.
14. Martin A. Green, K.E., Yoshihiro Hishikawa, Wilhelm Warta, Ewan D. Dunlop, Dean H. Levi and Anita W. Y. Ho-Baillie, *Solar cell efficiency table (version 49)*. Progress in photovoltaics, 2017. **25**.

15. Strandberg, R., *Detailed balance analysis of area de-coupled double tandem photovoltaic modules*. Applied Physics Letters, 2015. **106**(3): p. 033902.
16. König, D., et al., *Hot carrier solar cells: Principles, materials and design*. Physica E: Low-dimensional Systems and Nanostructures, 2010. **42**(10): p. 2862-2866.
17. Konovalov, I., V. Emelianov, and R. Linke, *Hot carrier solar cell with semi-infinite energy filtering*. Solar Energy, 2015. **111**: p. 1-9.
18. Conibeer, G., et al., *Modelling of hot carrier solar cell absorbers*. Solar energy materials and solar cells, 2010. **94**(9): p. 1516-1521.
19. Yao, Y. and D. König, *Comparison of bulk material candidates for hot carrier absorber*. Solar Energy Materials and Solar Cells, 2015. **140**: p. 422-427.
20. Limpert, S., S. Bremner, and H. Linke, *Reversible electron-hole separation in a hot carrier solar cell*. New Journal of Physics, 2015. **17**(9): p. 095004.
21. Ross, R.T. and A.J. Nozik, *Efficiency of hot-carrier solar energy converters*. Journal of Applied Physics, 1982. **53**(5): p. 3813-3818.
22. Brongersma, M.L., N.J. Halas, and P. Nordlander, *Plasmon-induced hot carrier science and technology*. Nature nanotechnology, 2015. **10**(1): p. 25-34.
23. Tisdale, W.A., et al., *Hot-electron transfer from semiconductor nanocrystals*. Science, 2010. **328**(5985): p. 1543-1547.
24. Luque, A. and A. Martí, *Increasing the efficiency of ideal solar cells by photon induced transitions at intermediate levels*. Physical Review Letters, 1997. **78**(26): p. 5014.
25. Datas, A., et al., *Intermediate band solar cell with extreme broadband spectrum quantum efficiency*. Physical review letters, 2015. **114**(15): p. 157701.
26. Luque, A., A. Martí, and C. Stanley, *Understanding intermediate-band solar cells*. Nature Photonics, 2012. **6**(3): p. 146-152.
27. Trupke, T., M. Green, and P. Würfel, *Improving solar cell efficiencies by up-conversion of sub-band-gap light*. Journal of Applied Physics, 2002. **92**(7): p. 4117-4122.
28. Wu, M., et al., *Solid-state infrared-to-visible upconversion sensitized by colloidal nanocrystals*. Nature Photonics, 2016. **10**(1): p. 31-34.
29. Trupke, T., M. Green, and P. Würfel, *Improving solar cell efficiencies by down-conversion of high-energy photons*. Journal of Applied Physics, 2002. **92**(3): p. 1668-1674.
30. Zhang, J., et al., *Efficient Quantum Cutting in Tb<sup>3+</sup>/Yb<sup>3+</sup> Codoped-NaYF<sub>4</sub> Single Crystals Grown by Bridgman Method Using KF Flux for Solar Photovoltaic*. IEEE Journal of Quantum Electronics, 2015. **51**(6): p. 1-6.

31. Briggs, J.A., A.C. Atre, and J.A. Dionne, *Narrow-bandwidth solar upconversion: Case studies of existing systems and generalized fundamental limits*. Journal of Applied Physics, 2013. **113**(12): p. 124509.
32. Yablonovitch, E., *Inhibited spontaneous emission in solid-state physics and electronics*. Physical review letters, 1987. **58**(20): p. 2059.
33. Wanlass, M., et al. *Recent Advances in Low-Bandgap, InP-Based GaInAs/InAsP Materials and Devices for Thermophotovoltaic (TPV) Energy Conversion*. in *AIP Conference Proceedings*. 2004. AIP.
34. Green, M.A., *Time-asymmetric photovoltaics*. Nano letters, 2012. **12**(11): p. 5985-5988.
35. Green, M.A., *Limiting photovoltaic efficiency under new ASTM International G173-based reference spectra*. Progress in Photovoltaics: Research and Applications, 2012. **20**(8): p. 954-959.
36. Zhao, J., et al., *19.8% efficient "honeycomb" textured multicrystalline and 24.4% monocrystalline silicon solar cells*. Applied Physics Letters, 1998. **73**(14): p. 1991-1993.
37. Masuko, K., et al., *Achievement of more than 25% conversion efficiency with crystalline silicon heterojunction solar cell*. IEEE Journal of Photovoltaics, 2014. **4**(6): p. 1433-1435.
38. Polman, A., et al., *Photovoltaic materials: Present efficiencies and future challenges*. Science, 2016. **352**(6283): p. aad4424.
39. Richter, A., M. Hermle, and S.W. Glunz, *Reassessment of the limiting efficiency for crystalline silicon solar cells*. IEEE journal of photovoltaics, 2013. **3**(4): p. 1184-1191.
40. Wang, X., et al., *Design of GaAs solar cells operating close to the Shockley–Queisser Limit*. IEEE Journal of Photovoltaics, 2013. **3**(2): p. 737-744.
41. Sai, H., et al., *11.0%-efficient thin-film microcrystalline silicon solar cells with honeycomb textured substrates*. IEEE J. Photovolt, 2014. **4**(6): p. 1349-1353.
42. Kayes, B.M., et al. *27.6% conversion efficiency, a new record for single-junction solar cells under 1 sun illumination*. in *Photovoltaic Specialists Conference (PVSC), 2011 37th IEEE*. 2011. IEEE.
43. Stanbery, B.J., *Copper indium selenides and related materials for photovoltaic devices*. Critical reviews in solid state and materials sciences, 2002. **27**(2): p. 73-117.
44. O'Regan, B. and M. Grätzel, *A low-cost, high-efficiency solar cell based on dye-sensitized*. nature, 1991. **353**(6346): p. 737-740.
45. Komiya, R., et al. *Improvement of the conversion efficiency of a monolithic type dye-sensitized solar cell module*. in *Technical Digest, 21st International Photovoltaic Science and Engineering Conference*. 2011.
46. You, J., et al., *Improved air stability of perovskite solar cells via solution-processed metal oxide transport layers*. Nature nanotechnology, 2016. **11**(1): p. 75-81.

47. Lee, M.M., et al., *Efficient hybrid solar cells based on meso-superstructured organometal halide perovskites*. Science, 2012. **338**(6107): p. 643-647.
48. Burschka, J., et al., *Sequential deposition as a route to high-performance perovskite-sensitized solar cells*. Nature, 2013. **499**(7458): p. 316-319.
49. Liu, M., M.B. Johnston, and H.J. Snaith, *Efficient planar heterojunction perovskite solar cells by vapour deposition*. Nature, 2013. **501**(7467): p. 395-398.
50. Jeon, N.J., et al., *Solvent engineering for high-performance inorganic-organic hybrid perovskite solar cells*. Nature materials, 2014. **13**(9): p. 897-903.
51. Yang, W.S., et al., *High-performance photovoltaic perovskite layers fabricated through intramolecular exchange*. Science, 2015. **348**(6240): p. 1234-1237.
52. Im, J.-H., et al., *Growth of CH<sub>3</sub>NH<sub>3</sub>PbI<sub>3</sub> cuboids with controlled size for high-efficiency perovskite solar cells*. Nature nanotechnology, 2014. **9**(11): p. 927-932.
53. Zhou, H., et al., *Interface engineering of highly efficient perovskite solar cells*. Science, 2014. **345**(6196): p. 542-546.
54. Yang, S., et al., *Above-bandgap voltages from ferroelectric photovoltaic devices*. Nature nanotechnology, 2010. **5**(2): p. 143-147.
55. Spanier, J.E., et al., *Power conversion efficiency exceeding the Shockley-Queisser limit in a ferroelectric insulator*. Nature Photonics, 2016.
56. Pérez-Tomás, A., M. Lira-Cantú, and G. Catalan, *Above-Bandgap Photovoltages in Antiferroelectrics*. Advanced Materials, 2016. **28**(43): p. 9644-9647.
57. Mori, S., et al. *Organic photovoltaic module development with inverted device structure*. in *Symposium U Organic Photovoltaics Fundamentals, Materials and Devices*. 2015. Cambridge Univ. Press.
58. Abelès, F., *VI methods for determining optical parameters of thin films*. Progress in optics, 1963. **2**: p. 249-288.
59. Wallentin, J., et al., *InP nanowire array solar cells achieving 13.8% efficiency by exceeding the ray optics limit*. Science, 2013. **339**(6123): p. 1057-1060.
60. Yao, M., et al., *Tandem solar cells using GaAs nanowires on Si: Design, fabrication, and observation of voltage addition*. Nano letters, 2015. **15**(11): p. 7217-7224.
61. Svensson, J., et al., *Diameter-dependent photocurrent in InAsSb nanowire infrared photodetectors*. Nano letters, 2013. **13**(4): p. 1380-1385.
62. Jain, V., et al., *Study of photocurrent generation in InP nanowire-based p+-i-n+ photodetectors*. Nano Research, 2014. **7**(4): p. 544-552.
63. Akasaki, I. and H. Amano, *Crystal growth and conductivity control of group III nitride semiconductors and their application to short wavelength light emitters*. Japanese journal of applied physics, 1997. **36**(9R): p. 5393.

64. Nakamura, S., T. Mukai, and M. Senoh, *Candela-class high-brightness InGaN/AlGaIn double-heterostructure blue-light-emitting diodes*. Applied Physics Letters, 1994. **64**(13): p. 1687-1689.
65. Duan, X., et al., *Single-nanowire electrically driven lasers*. Nature, 2003. **421**(6920): p. 241-245.
66. Greytak, A.B., et al., *Semiconductor nanowire laser and nanowire waveguide electro-optic modulators*. Applied Physics Letters, 2005. **87**(15): p. 151103.
67. Åberg, I., et al., *A GaAs nanowire array solar cell with 15.3% efficiency at 1 Sun*. IEEE Journal of Photovoltaics, 2016. **6**(1): p. 185-190.
68. Mariani, G., et al., *Direct-Bandgap Epitaxial Core–Multishell Nanopillar Photovoltaics Featuring Subwavelength Optical Concentrators*. Nano letters, 2013. **13**(4): p. 1632-1637.
69. Yu, S., F. Roemer, and B. Witzigmann, *Analysis of surface recombination in nanowire array solar cells*. Journal of Photonics for Energy, 2012. **2**(1): p. 028002-1-028002-9.
70. Wang, X., et al., *Performance-limiting factors for GaAs-based single nanowire photovoltaics*. Optics express, 2014. **22**(102): p. A344-A358.
71. van Dam, D., et al., *High-efficiency nanowire solar cells with omnidirectionally enhanced absorption due to self-aligned Indium–Tin–Oxide Mie scatterers*. ACS nano, 2016. **10**(12): p. 11414-11419.
72. Dimroth, F., et al., *Wafer bonded four-junction GaInP/GaAs//GaInAsP/GaInAs concentrator solar cells with 44.7% efficiency*. Progress in Photovoltaics: Research and Applications, 2014. **22**(3): p. 277-282.
73. Pan, D., et al., *Free-standing two-dimensional single-crystalline InSb nanosheets*. Nano letters, 2016. **16**(2): p. 834-841.
74. Anttu, N., *Geometrical optics, electrostatics, and nanophotonic resonances in absorbing nanowire arrays*. Optics letters, 2013. **38**(5): p. 730-732.
75. Heurlin, M., et al., *Axial InP nanowire tandem junction grown on a silicon substrate*. Nano letters, 2011. **11**(5): p. 2028-2031.
76. Lee, C.H., D.R. Kim, and X. Zheng, *Fabricating nanowire devices on diverse substrates by simple transfer-printing methods*. Proceedings of the National Academy of Sciences, 2010. **107**(22): p. 9950-9955.
77. Heurlin, M., et al., *Continuous gas-phase synthesis of nanowires with tunable properties*. Nature, 2012. **492**(7427): p. 90-94.
78. Wagner, R. and W. Ellis, *Vapor-liquid-solid mechanism of single crystal growth*. Applied Physics Letters, 1964. **4**(5): p. 89-90.
79. Chang, C.-C., et al., *Electrical and optical characterization of surface passivation in GaAs nanowires*. Nano letters, 2012. **12**(9): p. 4484-4489.
80. Nowzari, A., et al., *A Comparative Study of Absorption in Vertically and Laterally Oriented InP Core–Shell Nanowire Photovoltaic Devices*. Nano letters, 2015. **15**(3): p. 1809-1814.
81. Jackson, J.D., *Classical electrodynamics*. 1999: Wiley.

82. Anttu, N. and H. Xu, *Scattering matrix method for optical excitation of surface plasmons in metal films with periodic arrays of subwavelength holes*. Physical Review B, 2011. **83**(16): p. 165431.
83. Persson, C., et al., *First-principle calculations of the dielectric function of zinc-blende and wurtzite InN*. Journal of Physics: Condensed Matter, 2001. **13**(40): p. 8945.
84. Law, S., et al., *Mid-infrared designer metals*. Optics express, 2012. **20**(11): p. 12155-12165.
85. Moharam, M., et al., *Formulation for stable and efficient implementation of the rigorous coupled-wave analysis of binary gratings*. JOSA a, 1995. **12**(5): p. 1068-1076.
86. Anttu, N., et al., *Optical far-field method with subwavelength accuracy for the determination of nanostructure dimensions in large-area samples*. Nano letters, 2013. **13**(6): p. 2662-2667.
87. Okamoto, K., *Fundamentals of optical waveguides*. 2010: Academic press.
88. Wang, B. and P.W. Leu, *Tunable and selective resonant absorption in vertical nanowires*. Optics letters, 2012. **37**(18): p. 3756-3758.
89. Anttu, N. and H. Xu, *Efficient light management in vertical nanowire arrays for photovoltaics*. Optics express, 2013. **21**(103): p. A558-A575.
90. Zhu, L. and S. Fan, *Near-complete violation of detailed balance in thermal radiation*. Physical Review B, 2014. **90**(22): p. 220301.
91. Han, S., *Theory of thermal emission from periodic structures*. Physical Review B, 2009. **80**(15): p. 155108.
92. Landau, L.D. and E. Lifshitz, *Statistical physics, part I*. 1980, Pergamon, Oxford. p. 187-188.
93. Anttu, N., *Shockley–Queisser detailed balance efficiency limit for nanowire solar cells*. ACS Photonics, 2015. **2**(3): p. 446-453.
94. Esaki, L., *New phenomenon in narrow germanium p– n junctions*. Physical review, 1958. **109**(2): p. 603.
95. Van Zeghbroeck, B., *Principles of semiconductor devices*. Colorado University, 2004.
96. Kivisaari, P., et al., *Monte Carlo simulation of hot carrier transport in III–N LEDs*. Journal of Computational Electronics, 2015. **14**(2): p. 382-397.
97. Hall, R.N., *Electron–hole recombination in germanium*. Physical Review, 1952. **87**(2): p. 387.
98. Huang, N., C. Lin, and M.L. Povinelli, *Limiting efficiencies of tandem solar cells consisting of III–V nanowire arrays on silicon*. Journal of Applied Physics, 2012. **112**(6): p. 064321.
99. LaPierre, R., *Theoretical conversion efficiency of a two-junction III–V nanowire on Si solar cell*. Journal of applied physics, 2011. **110**(1): p. 014310.
100. Christesen, J.D., et al., *Design principles for photovoltaic devices based on Si nanowires with axial or radial p–n junctions*. Nano letters, 2012. **12**(11): p. 6024-6029.

101. Gabriel, M.M., et al., *Imaging charge separation and carrier recombination in nanowire pin junctions using ultrafast microscopy*. Nano letters, 2014. **14**(6): p. 3079-3087.
102. Gutsche, C., et al., *Direct determination of minority carrier diffusion lengths at axial GaAs nanowire p–n junctions*. Nano letters, 2012. **12**(3): p. 1453-1458.
103. Joyce, H.J., et al., *Ultralow surface recombination velocity in InP nanowires probed by terahertz spectroscopy*. Nano letters, 2012. **12**(10): p. 5325-5330.
104. <http://www.ioffe.ru/SVA/NSM/Semicond/InP/electric.html#Hall>.
105. Allen, J.E., et al., *High-resolution detection of Au catalyst atoms in Si nanowires*. Nature nanotechnology, 2008. **3**(3): p. 168-173.
106. Dan, Y., et al., *Dramatic reduction of surface recombination by in situ surface passivation of silicon nanowires*. Nano letters, 2011. **11**(6): p. 2527-2532.
107. Anttu, N., *Modifying the emission of light from a semiconductor nanowire array*. Journal of Applied Physics, 2016. **120**(4): p. 043108.
108. Song, B., *Probing Radiative Thermal Transport at the Nanoscale*. 2015.
109. Niv, A., et al., *Near-field electromagnetic theory for thin solar cells*. Physical review letters, 2012. **109**(13): p. 138701.
110. Palik, E.D., *Handbook of Optical Constants of Solids (Academic, Orlando, 1985)*. Google Scholar: p. 286-297.



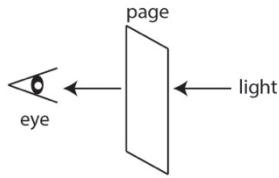


**Figure.** Instructions for reading the dedication pages. These two dedication pages should be printed on both sides of a blank G5 paper. The reader should hold them up to the light.

The citation is from the book, ‘The God particle: If the universe is the answer, what is the question?’ by L. M. Lederman and D. Teresi, Dell Publishing (1993).